Journal of Applied and Computational Mechanics

Shahid Chamran University of Ahvaz

Stagnation Point Hybrid Nanofluid Flow and Entropy Production with Influence of Nonlinear Thermal Convection on a Riga Plate with Application of Neural Network Technique

Hamdi Ayed[1], Arshad Khan[2], Taza Gul[3], Abir Mouldi[4], Hamiden Abd El-Wahed Khalifa[5,6], Agaeb Mahal Alanzi[5]

[1] Department of Civil Engineering, College of Engineering, King Khalid University, Abha – 61421, Saudi Arabia, Email: hayed@kku.edu.sa

[2] College of Aeronautical Engineering, National University of Sciences and Technology (NUST), Sector H-12, Islamabad 44000, Pakistan, Email: arshad8084@gmail.com

[3] Department of Mathematics, City University of Science and Information Technology, Peshawar 25000, Pakistan, Email: tazagul@cusit.edu.pk

[4] Department of Industrial Engineering, College of Engineering, King Khalid University, Abha – 61421, Saudi Arabia, Email: amouldi@kku.edu.sa

[5] Department of Mathematics, College of Science, Qassim University, Buraydah, 51452, Saudi Arabia

[6] Department of Operations and Management Research, Faculty of Graduate Studies for Statistical Research, Cairo University, Giza 12613, Egypt, Email: Ha.Ahmed@qu.edu.sa

Abstract. This study examines the generation of irreversibility and the behavior of stagnation point hybrid nanofluid flow on a Riga plate. The effects of nonlinear thermally convective and solar radiation are incorporated in the modeled equations. The nanoparticles of (Cu) and (Al_2O_3) are mixed with Glycol ($C_3H_8O_2$) to hybridized it. The leading equations have been changed to dimension-free form by using the set of appropriate variables and then have been evaluated by Artificial Neural Network (ANN) approach. It is revealed in this work that, the velocity panels are amplified with expansion in Grashof number and electromagnetic factor while declined with escalation in magnet/electrode factor and nanoparticles concentration. Upsurge, in Eckert number for both the scenarios ($Ec < 0$) and ($Ec > 0$), the radiation factor and nanoparticles concentration cause augmentation in thermal characteristics. Radiation factor has positive impacts on Bejan number and generation of Entropy. Moreover, Bejan number is retarded while entropy is augmented with growth in Brinkman number. It is also established in this work that the principle of entropy generation for hybrid nanoparticles supports the efficient delivery of drug in cancer treatment.

Keywords: Nanofluidics; Artificial neural network; Entropy generation; Casson fluid Nonlinear convection; Thermal radiation.

1. Introduction

Nanofluid flow involves the motion of a suspension encompassing nanoparticles within a pure fluid initially proposed by Choi [1]. This blend of nanoparticles and the pure fluid modifies the thermal and flow attributes of the compound. The mixed nanoparticles, owing to their minute dimensions, frequently demonstrate distinctive traits like heightened thermal conductivity, profoundly influencing the collective fluid dynamics and heat transfer efficacy [2]. This improvement is particularly beneficial in applications where heat dissipation is crucial, like in cooling systems for electronics or heat exchangers. Hashemi-Tilehnoee et al. [3] analyzed natural convective nanofluid flow through a conduit using thermal radiations and magnetic effects. Seyyedi et al. [4] discussed thermally radiative and naturally convective Alumina-water nanofluid flow with electric field effects. The presence of nanoparticles alters the fluid's behavior, promoting convective currents and enhancing heat transfer rates [5]. This phenomenon is particularly advantageous in applications like solar thermal systems and automotive cooling, where efficient heat transfer is essential for optimal performance [6]. Dogonchi et al. [7] examined the impression of thermal source on the MHD flow of nanofluid on an extending sheet, incorporating heterogeneous/homogeneous reactions alongside thermally radiative effects. With the passage of time, it has revealed that the mixing of two distinct kind of nanoparticles in a pure fluid is termed as hybrid nanofluid. Over time, it has become apparent that the combination of two different types of nanoparticles within a pure fluid is referred to as a hybrid nanofluid. This term denotes a deliberate blending process where nanoparticles of varying compositions or properties are dispersed evenly throughout the base fluid [8]. Hybrid nanofluids represent a strategic approach to tailoring the thermal and flow characteristics of the fluid medium, capitalizing on the unique attributes of each nanoparticle type [9]. By mixing nanoparticles with diverse sizes, shapes, or materials, engineers can achieve desired enhancements in thermal

conductivity, convective heat transfer, and other relevant properties [10]. This deliberate combination allows for the creation of nanofluids with tailored behaviors suited to specific applications, from advanced cooling systems to biomedical technologies [11]. As research in this field progresses, the understanding of hybrid nanofluids continues to evolve, unlocking new possibilities for optimizing heat transfer efficiency and performance across various engineering disciplines.

Entropy is a concept from thermodynamics that measures the amount of disorder in the system. Khan et al. [12] scrutinized the augmentation of thermal transportation and generation of entropy for a titanium based nanofluid flow on a permeable surface. Fluid flow with analysis of entropy involves a comprehensive examination of the thermodynamic behavior of fluids in motion, considering the changes in entropy within the system. In fluid dynamics, entropy analysis provides valuable insights into the irreversibilities and energy losses associated with fluid flow processes [13]. Hashemi-Tilehnoee et al. [14] have used production of entropy for main transmission lines. Khan et al. [15] studied generation of entropy for fractional order nanofluid flow on a permeable sheet using the impacts of wall heating and slip constraints. The study of entropy generation within fluid flow systems is essential for understanding the inefficiencies and optimizing the performance of various engineering applications, including heat exchangers, turbomachinery, and propulsion systems [16]. By quantifying entropy generation rates and analyzing entropy balances, engineers can identify opportunities to minimize irreversible processes, enhance energy efficiency, and improve overall system performance. Furthermore, entropy analysis facilitates the assessment of system reliability, enabling the development of robust fluid flow solutions that meet stringent performance requirements while minimizing environmental impacts [17]. Overall, integrating entropy considerations into fluid flow analysis enhances our understanding of the thermodynamic principles governing fluid behavior and enables the design of more efficient and sustainable engineering systems. Khan et al. [18] examined generalized various slip constraints and entropy generation for Casson fluid flow with fractional derivatives.

Casson fluid, a non-Newtonian fluid model, is characterized by its yield stress and shear-thinning behavior. In Casson fluid flow analysis, the fluid's velocity profile deviates from classical Newtonian fluids due to the presence of yield stress, where flow initiation requires a certain stress threshold. This unique behavior influences heat transfer phenomena profoundly. Khan et al. [19] studied Casson fluid flow on an inclined surface using generalized Fick's and Fourier Laws and have also analyzed the generation of entropy in their study. In case of Casson fluid flow the non-linear velocity profile alters the convective heat transfer characteristics near solid boundaries, affecting the rate of heat transfer [20]. Additionally, the yield stress induces the formation of yield surfaces, which can lead to flow separation and reattachment phenomena, altering the heat transfer patterns. Furthermore, the shear-thinning behavior affects the boundary layer development and thickness, impacting the thermal layer at boundary and consequently altering the rate of heat transfer [21]. Casson fluid's rheological properties also affect the onset of instabilities such as thermal convection, which further modifies the heat transfer characteristics [22]. In applications such as food processing, biomedical engineering, and polymer processing where Casson fluids are common, understanding these impacts is crucial for optimizing process efficiency and product quality [23]. Computational fluid dynamics simulations coupled with heat transfer analysis provide insights into these complex interactions, aiding in the design and optimization of systems involving Casson fluid flow for enhanced heat transfer performance [24]. Additionally, experimental studies utilizing advanced visualization techniques offer validation and further understanding of Casson fluid behavior and its impacts on heat transfer. Overall, the study of Casson fluid flow and its effects on heat transfer presents a challenging yet essential area of research with diverse applications like industrial processes to biomedical applications, and nuclear reactors promising advancements in various fields [25].

Nonlinear convection refers to fluid flow phenomena where the flow pattern deviates significantly from the simple, linear behavior observed in laminar flows. In nonlinear convection, the fluid motion is influenced by complex interactions between inertia, viscosity, and buoyancy forces, often leading to the formation of intricate flow structures and patterns. This phenomenon greatly impacts heat transfer processes by altering flow characteristics and heat transfer rates in various systems [26]. In nonlinear convection, the formation of secondary flows, flow instabilities, and transitions to turbulence significantly affect heat transfer mechanism. For instance, in natural convection, where buoyancy forces drive fluid motion, nonlinear effects lead to the formation of convective cells and boundary layer instabilities, which enhance heat transfer rates near solid surfaces [27, 28]. In turbulent flows, characterized by chaotic and unpredictable motion, nonlinear convection enhances mixing and transport processes, promoting heat transfer through increased turbulent diffusion. Additionally, in flows involving highly viscous or non-Newtonian fluids, nonlinear effects influence flow resistance and boundary layer development, altering thermal boundary layer thickness and heat transfer rates [29]. Understanding and predicting nonlinear convection phenomena are essential for optimizing heat transfer performance in engineering applications such as thermal management systems, and industrial processes, where efficient heat transfer is critical for system operation and performance optimization [30]. Various numerical simulations, advanced mathematical modeling, and experimental studies play pivotal roles in elucidating the complexities of nonlinear convection and its impacts on heat transfer, enabling engineers and researchers to develop more efficient and reliable heat transfer systems across various industries.

Artificial Neural Network (ANN) is a machine learning approach motivated by the working and configuration of human brain. Comprised of interrelated nodes called neurons, arranged in layers, ANNs process complex data inputs to produce desired outputs through a process called forward propagation [31, 32]. Through a training process involving optimization algorithms like gradient descent, ANNs adjust their internal parameters to reduce the alteration between expected and concrete outputs, using backpropagation [33]. ANNs have demonstrated remarkable success across various tasks like autonomous driving, making them a foundational component of modern artificial intelligence systems. Among optimization methodologies utilized in the training of artificial neural networks (ANNs), the Levenberg–Marquardt supervised neural networks algorithm (LMS-NNA) stands as a sophisticated and widely employed approach [33]. Originally developed for nonlinear least squares problems, LMS-NNA has found extensive application in the realm of training ANNs due to its ability to efficiently adjust network parameters while minimizing the error between predicted and actual outputs [34]. Unlike traditional gradient descent methods, LMS-NNA incorporates second-order information about the error surface, enabling it to adaptively adjust the step size and direction of parameter updates. This feature facilitates faster convergence, particularly in scenarios with high-dimensional parameter spaces. By combining aspects of gradient descent and the Gauss-Newton method, LMS-NNA strikes a balance between computational efficiency and robustness, making it well-suited for training ANNs in diverse domains [35]. Additionally, its ability to handle noisy data and ill-conditioned problems further enhances its utility in practical applications [36, 37]. Through an iterative process of updating network weights and biases based on the curvature of the error surface, LMS-NNA effectively navigates towards optimal solutions, thereby improving the performance and generalization capabilities of ANNs [38]. Its versatility and effectiveness have positioned LMS-NNA as a cornerstone optimization technique in the field of neural network training, contributing significantly to advancements in artificial intelligence and machine learning research. Aljohani et al. [39] used LMS-NNA (ANN) to pretend a system's behavior of a coating wire concerning fluid flow on a sheet, while Sulaiman et al. [40] analyzed thermal transport characteristics in fluid flow over surfaces using supervised neural network techniques.
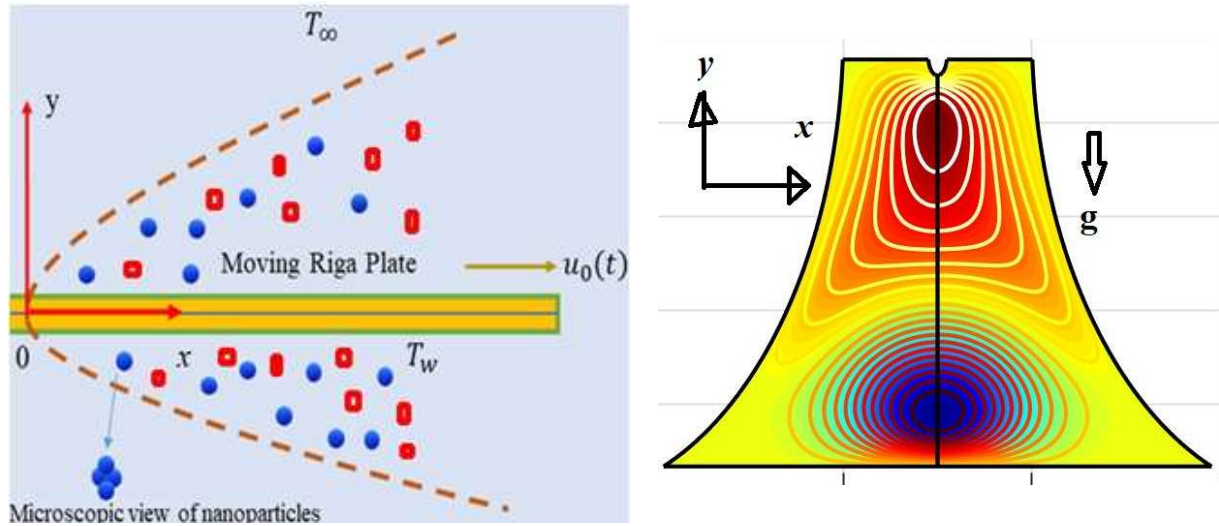
Fig. 1. The schematic view of flow problem.

From the literature survey, it is revealed that no data is available regarding the nonlinear thermally convective unsteady Casson hybrid nanofluid flow on a Riga plate with implication of artificial neural network (ANN) that created a gap in the exiting literature. To fill the gap, this study examines the generation of irreversibility and the behavior of stagnation point flow on a Riga plate. The effects of nonlinear thermal convective and solar radiative are incorporated in the model. The nanoparticles of (Cu) and (Al_2O_3) are mixed with Glycol ($C_3H_8O_2$) to hybridized it. The leading equations are evaluated by ANN approach.

2. Problem Formulation

Assume a stagnation point flow of a Casson hybrid nanofluid on a Riga plate, where copper and aluminum oxide nanoparticles are suspended in glycol, serving as the base fluid. Flow of fluid is based on time and is impacted by nonlinear thermal convection, solar radiations and viscous dissipation. The plate is stretched with velocity $u_w = b(x - x_0)/(t_{ref} - \beta t)$ such that $b > 0$. Wall and ambient temperatures are respectively depicted as T_w, T_∞ (see Fig. 1). The application of the Lorentz force seeks to reduce turbulence in the flow field and improve the thermal distribution. Free steam velocity is described as $u_e = \alpha(t_{ref} - \beta t)^{-1}(x - x_0)$ where $\alpha, t_{ref}, t, \beta$ are, respectively, the acceleration factor, reference time, time and unsteadiness factor. When $\beta = 0$, we have steady flow, for $\beta > 0$, the flow is unsteady for $\beta < \beta_0$ $(\beta_0 > 0)$, the flow is unsteady and decelerating.

Using above assumptions, we have [41-43]:

$$\frac{\partial u}{\partial x} + \frac{\partial v}{\partial y} = 0,\tag{1}$$

$$\rho_{hnf}\left(\frac{\partial u}{\partial t} + u\frac{\partial u}{\partial x} + v\frac{\partial u}{\partial y}\right) = \mu_{hnf}\left(1 + \frac{1}{\beta}\right)\left(\frac{\partial^2 u}{\partial y^2} + \frac{\partial u_e}{\partial t} + u_e\frac{\partial u_e}{\partial x}\right) + \left(\frac{\pi j_0 M_0}{8}\right)e^{\left(\frac{-\pi y_1}{p}\right)} + g(\beta_{T^\rho})_{hnf}(T - T_\infty) + g(\beta_{T^\rho}^2)_{hnf}(T - T_\infty)^2,\tag{2}$$

$$\frac{\partial T}{\partial t} + u\frac{\partial T}{\partial x} + v\frac{\partial T}{\partial y} = \left(\frac{k_{hnf}}{(\rho c_p)_{hnf}}\right)\left(\frac{\partial^2 T}{\partial y^2}\right) + \left(\frac{\mu_{nf}}{(\rho c_p)_{nf}}\right)\left(\frac{\partial u}{\partial y}\right)^2 - \left(\frac{1}{(\rho c_p)_{hnf}}\right)\left(\frac{\partial q}{\partial y}\right).\tag{3}$$

The subjected constraints are:

$$u(0) = u_w, \quad T(0) = T_w, \quad v(0) = 0, \quad T(\infty) = T_\infty, \quad u(\infty) = u_e.\tag{4}$$

Mathematical representation of the solar thermal radiation q_r is provided as [44]:

$$q_r = -\frac{4}{3}\frac{\sigma^\cdot}{k^\cdot}\frac{\partial T^4}{\partial y}\tag{5}$$

Variables of similarity form are described as:

$$u = \left(\frac{\alpha(x - x_0)}{t_{ref} - t\beta}\right)f'(\eta), \quad v = -\alpha\left(\sqrt{\frac{v_f}{t_{ref} - t\beta}}\right)f(\eta), \quad \eta = \frac{y}{\sqrt{v_f(t_{ref} - \beta t)}}, \quad \Theta(\eta) = \frac{T - T_\infty}{T_w - T_\infty}.\tag{6}$$

Using Eqs. (5) and (6), we have from Eqs. (1) to (4) as:

$$f''' + \alpha\left(\frac{\rho_{hnf}}{\rho_f}\frac{\mu_f}{\mu_{hnf}}\right)\left(1 + \frac{1}{\beta}\right)\left[ff'' + 1 - S\left(\left(\frac{\eta}{2}\right)f'' + f' - 1 - (f')^2\right)\right] + MH\left(\frac{\mu_f}{\mu_{hnf}}\right)\exp(-\Lambda\eta) + Gr^\cdot\Theta^2 + Gr\Theta = 0,\tag{7}$$

$$\Theta''\left(\frac{k_{hnf}}{k_f} + \frac{4}{3}Rd\right) + Pr\frac{(\rho c_p)_{hnf}}{(\rho c_p)_f}\left[\alpha f\Theta' - \frac{S\eta}{2}\Theta'\right] + Ec\left(\frac{\mu_f}{\mu_{hnf}}\right)(f')^2 = 0,\tag{8}$$

Table 1. Numerical values of Al_2O_3, Cu and $C_3H_8O_2$ as depicted in Ref. [45].

Physical characteristics	Al_2O_3	$C_3H_8O_2$	Cu
k (W/mK)	40	34.5	400
c_p (J/kg.K)	765	4338	385
ρ (kg/m³)	3970	5060	8933
β (1/K)	0.85	0.00062	1.67
σ (s/m)	35×10^6	0.5×10^6	59.6×10^6

The boundary constraints associated with the problem are:

$$f(0) = 0, \ \Theta(0) = 1, \ f'(0) = c, \ \Theta(\infty) = 0, \ f'(\infty) = 1. \tag{9}$$

In Eq. (9), $c = b/\alpha$ is a fixed rate with $\alpha > 0$, in addition, we have some main factors which are mathematically described as: $Pr = \mu C_P / k_f = $ Prandtl number, $Rd = 4\sigma^* T_\infty^3 / k^* k_f = $ radiation factor, $S = \beta / \alpha = $ unsteadiness factor, $Gr = g(\beta_T)(T_w - T_\infty)x^3 / v_f^2 = $ Grashof number, $\Lambda = \pi\sqrt{v_f} / p = $ width factor for electrode/magnet. $Ec = u_w^2 / (C_p)_f (T_w - T_\infty) = $ Eckert number, $Gr^* = g(\beta_T^2)(T_w - T_\infty)^2 x^3 / v_f^2 = $ nonlinear Grashof number and $MH = \pi j_0 M_0 / 8\alpha\rho_f = $ EMHD Riga plate factor.

2.1. Thermo-physical properties

Assume that $\phi_{Cu} = $ copper volume fraction, while $\phi_{Al2O3} = $ alumina volume fraction for description of thermos-physical features of nanoparticles. Table 1 demonstrates the numerical values of these properties as derived from Ref. [45].

$$\frac{\rho_{hnf}}{\rho_f} = (1 - \phi_{Cu})\left[\frac{\rho_{Al2O3}}{\rho_f}\phi_{Al2O3} + (1 - \phi_{Al2O3})\right] + \phi_{Cu}\frac{\rho_{Cu}}{\rho_f},$$

$$\frac{\mu_{hnf}}{\mu_f} = \frac{1}{(1 - \phi_{Al2O3})^{2.5}(1 - \phi_{Cu})^{2.5}},$$

$$\frac{(\rho cp)_{hnf}}{(\rho cp)_f} = (1 - \phi_{Cu})\left[(1 - \phi_{Al2O3}) + \phi_{Al2O3}\frac{(\rho cp)_{Al2O3}}{(\rho cp)_f}\right] + \phi_{Cu}\frac{(\rho cp)_{Cu}}{(\rho cp)_f},$$

$$\frac{\sigma_{hnf}}{\sigma_{nf}} = \frac{(1 + 2\phi_{Al2O3})\sigma_{Al2O3} + (1 - 2\phi_{Al2O3})\sigma_{nf}}{(1 - \phi_{Al2O3})\sigma_{Cu} + (1 + \phi_{Al2O3})\sigma_{nf}}, \tag{10}$$

$$\frac{\sigma_{nf}}{\sigma_f} = \frac{\sigma_{Cu}(2\phi_{Cu} + 1) + (1 - 2\phi_{Cu})\sigma_f}{\sigma_{Cu}(1 - \phi_{Cu}) + (\phi_{Cu} + 1)\sigma_f},$$

$$\frac{k_{nf}}{k_f} = \left(\frac{k_{Al2O3} + 2k_{nf} - (k_{nf} - k_{Al2O3})2\phi_{Al2O3}}{k_{Al2O3} + 2k_{nf} + (k_{nf} - k_{Al2O3})\phi_{Al2O3}}\right),$$

$$\frac{k_{nf}}{k_f} = \left(\frac{k_{Cu} + 2k_f - 2\phi_{Cu}(k_f - k_{Cu})}{k_{Cu} + 2k_f + \phi_{Cu}(k_f - k_{Cu})}\right),$$

2.2. Simulation of Cu-Al_2O_3/$C_3H_8O_2$ nanofluid

The thermo-physical characteristics of k_{hnf} and μ_{hnf} as outlined in Ref. [45], are illustrated as follows:

$$\frac{k_{hnf}}{k_f} = (306\phi_{Al2O3}^2 - 0.19\phi_{Al2O3} + 1)(306\phi_{Cu}^2 - 0.19\phi_{Cu} + 1), \tag{11a}$$

$$\frac{\mu_{hnf}}{\mu_f} = (306\phi_{Al2O3}^2 - 0.19\phi_{Al2O3} + 1)(306\phi_{Cu}^2 - 0.19\phi_{Cu} + 1). \tag{11b}$$

2.3. Interested quantities

The quantities of interest regarding skin friction and Nusslet number are described in mathematical form as:

$$Cf = \frac{\tau_w}{\rho_{hnf} u_e^2}, \tau_w = \mu_{hnf}\left(\frac{\partial u}{\partial y}\right)_{y=0} \tag{12}$$

Using Eq. (6) in Eq. (12), we have:

$$R_e^{0.5}Cf = \left(\frac{\mu_{hnf}}{\mu_f}\right)f''(0) \tag{13}$$

$$Nu_x = \frac{xq_w}{k_f(T_w - T_0)}, \ q_w = -\left[k_{hnf} + \frac{16\sigma^* T_\infty^3}{3k^*}\right]\left(\frac{\partial T}{\partial y}\right)_{y=0}, \tag{14}$$
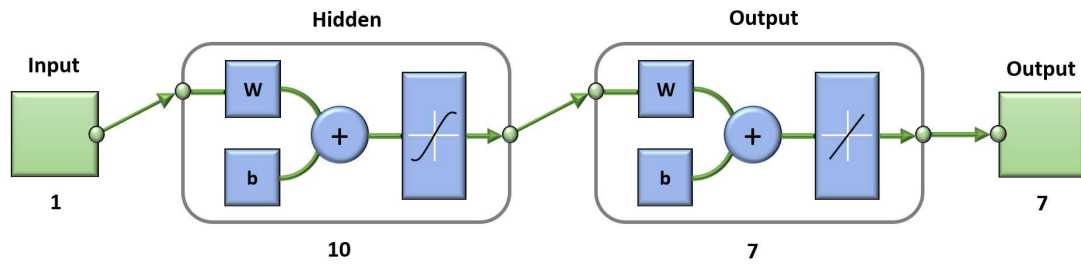
Fig. 2. The model problem employs a layered distribution, incorporating the stagnation point.

Using Eq. (6) in Eq. (14), we have:

$$R_e^{-0.5} Nu_x = -\left(\left(\frac{4}{3}\right)Rd + \frac{k_{hnf}}{k_f}\right)\Theta'(0). \tag{15}$$

3. Generation of Entropy

Entropy, a thermodynamic feature, quantifies the extent of disorder within a system, reflecting the dispersion of energy and the microscopically possible arrangements of the system. Essentially, it signifies the thermal energy within a system unavailable for work. Entropy's significance lies in the second law of thermodynamics, asserting that the entire entropy of isolated system invariably rises with time. In the current context, its mathematical expression is presented as [46-48]:

$$S_g = \left(\frac{1}{T_\infty^2}\right)\left(k_{hnf} + \frac{16T_h^3\sigma^*}{3k^*}\right)\left(\frac{\partial T}{\partial y}\right)^2 + \left(\frac{\mu_{hnf}}{T_\infty}\right)\left(1 + \frac{1}{\beta}\right)\left(\frac{\partial u}{\partial y}\right)^2, \tag{16}$$

Using Eq. (6), we have from Eq. (16) [46-48]:

$$S_G = \left(\frac{k_{hnf}}{k_f} + \frac{4}{3}Rd\right)\lambda(\Theta')^2 + Br\left(1 + \frac{1}{\beta}\right)\left[(f'')^2 (1 - \phi_{Cu})^{-2.5} (1 - \phi_{Al2O3})^{-2.5}\right]. \tag{17}$$

In above equation, $S_G = S_g T_\infty / (T_w - T_\infty)$ while $\lambda = (T_w - T_\infty)/T_\infty$ depicts the difference in entropy rate and temperatures.

3.1. Bejan Number

It is a dimensionless quantity that is defined as [46-48]:

$$Be = \frac{\frac{k_{hnf}}{k_f}\lambda(\Theta')^2}{\lambda\left(\frac{k_{hnf}}{k_f} + Rd\right)(\Theta')^2 + \left(1 + \frac{1}{\beta}\right)Br\left[(f'')^2 (1 - \phi_2)^{-2.5} (1 - \phi_1)^{-2.5}\right]}. \tag{18}$$

4. Method of Solution

The multilayer perceptron (MLP) network stands as one of the most prevalent artificial neural network (ANN) models utilized across various fields. Within its architecture, the LMS-NNA (Levenberg-Marquardt Learning Algorithm with Backpropagation Neural Network) plays a pivotal role in gathering and preserving information throughout the learning process. The LMS-NNA, a combination of the Levenberg-Marquardt Learning Algorithm and Backpropagation Neural Network, plays a crucial role in optimizing the MLP network's performance during the learning phase. Backpropagation, a fundamental algorithm in neural network training, involves iteratively adjusting the network's weights based on the error between predicted and actual outputs. This process allows the network to gradually improve its performance over time by minimizing prediction errors. The Levenberg-Marquardt Learning Algorithm enhances the traditional backpropagation method by introducing adaptive learning rates. This adaptive nature enables the algorithm to converge more quickly towards optimal solutions while maintaining stability during training. By dynamically adjusting learning rates based on the network's performance, the Levenberg-Marquardt algorithm accelerates the learning process and mitigates the risk of getting stuck in local minima. This study examines the generation of irreversibility and the behavior of stagnation point hybrid nanofluid flow on a Riga plate. The effects of nonlinear thermal convection and solar radiation are incorporated in flow problem. The nanoparticles of (Cu) and (Al_2O_3) are mixed with Glycol ($C_3H_8O_2$) to hybridized it. Figure 2 illustrates the ANN approach, utilizing an algorithmic approach to optimize LMS-NNA design and assess Mean Squared Error (MSE) performance.

5. Computational Results with Detailed Explanation

Figures 3a to 3e depict the LMS-NNA design influence of EMHD Riga surface factor (M_H) on $f'(\eta)$, accompanied by the analysis of curve fitting. As (M_H) escalates the retardation in $f'(\eta)$ is observed for mono and hybrid nanofluids as depicted in Figs. 3a and 3c. This phenomenon can be interpreted physically in the context of electromagnetically driven fluid dynamics. The Riga plate factor represents a parameter associated with the electromagnetic forces acting on the fluid. With growth (M_H), these electromagnetic forces become more dominant within the system. Consequently, $f'(\eta)$, which describes the spatial variation of fluid velocities, experiences retardation. This slowdown can be attributed to the increased resistance encountered by the fluid particles due to the amplified electromagnetic forces, leading to a decrease in the overall fluid velocity across the distribution. This interpretation highlights the complex relationship between electromagnetic fields and fluid motion, demonstrating how changes in (M_H) influence the dynamic behavior of the fluid system. The error analysis associated with velocity profiles against

variations in (M_H) is depicted in Figs. 3b and 3d. In fluid dynamics and magnetic field scenarios, error analysis constitutes a crucial step in assessing the reliability and accuracy of predictive models. It involves a quantitative scrutiny of the differences between predicted and observed velocity profiles, aimed at evaluating the fidelity of the current model. In our model, absolute error values are meticulously examined, with these values falling within range 10^{-7} to 10^{-3} corresponding to the configurations of their respective artificial neural networks (ANNs). These numerical findings serve as a vital metric for gauging the performance of the models. When juxtaposed with reference outputs obtained from theoretical data, the error analysis confirms the commendable level of accuracy within the specified range given by 10^{-7} to 10^{-3}, thus validating the efficacy of the designed ANN models. This rigorous validation process underscores the significance of error analysis in ensuring the reliability and robustness of predictive models in fluid dynamics and magnetic field scenarios, thereby enhancing confidence in their applicability and utility across various domains. Figure 3e centers on curve fitting analysis, a statistical technique used to find the best-fit curve for a set of data points. This figure delves into curve fitting analysis, a statistical methodology employed to identify the optimal curve that closely aligns with a given set of data points. Within the context of the discussion, this technique serves as a powerful tool for evaluating the consistency between the mathematical model and the observed velocity profiles as the parameter varies. Essentially, Fig. 3e offers a visual representation of how well the mathematical model captures the behavior of the observed velocity profiles across variations in (M_H).
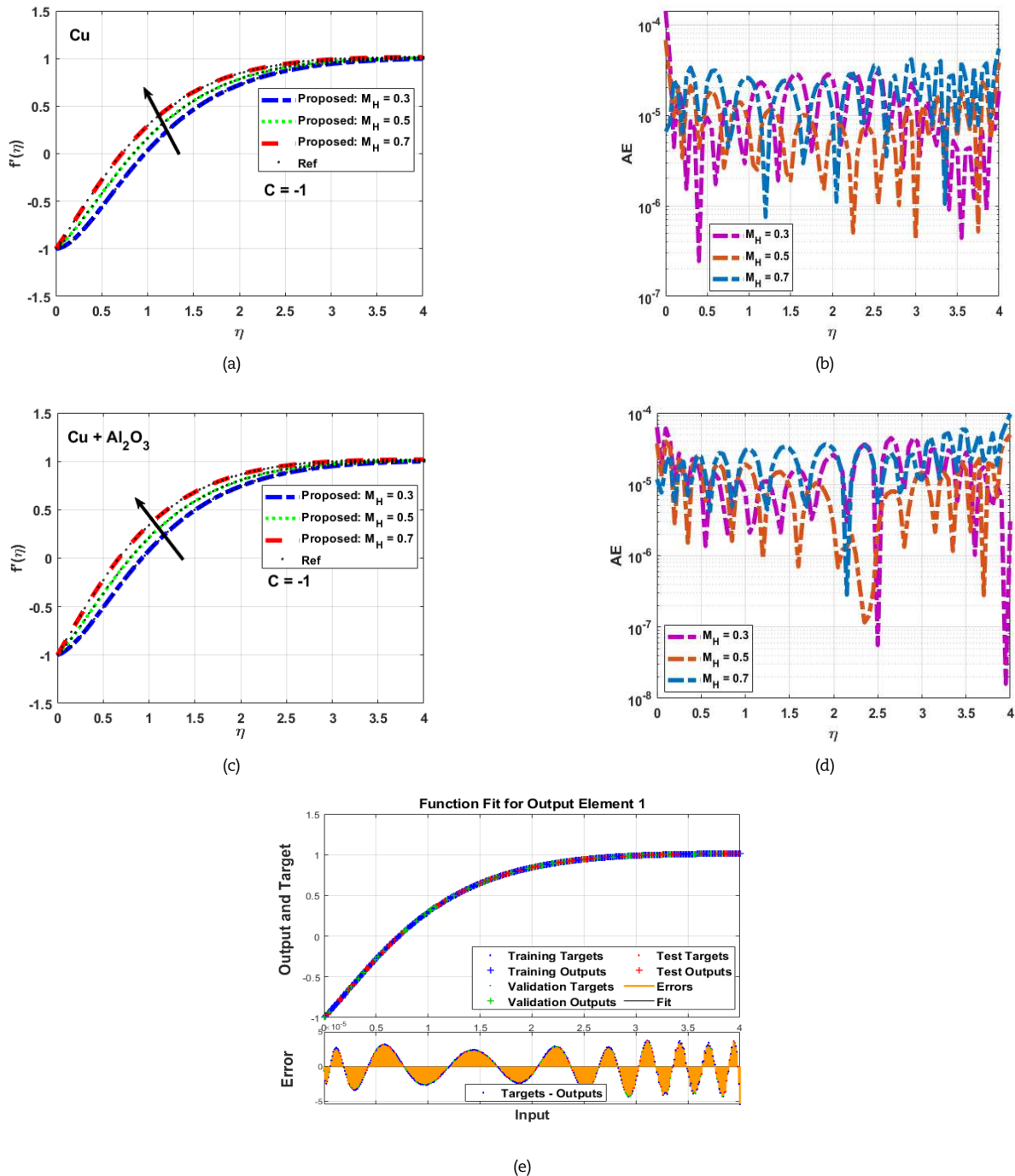

(a)

(b)

(c)

(d)

(e)

Fig. 3. Impacts of (M_H) on $f'(\eta)$ with curve fitting analysis: (a) behavior of $f'(\eta)$ vs (M_H) with ANN, (b) AE vs (M_H), (c) behavior of $f'(\eta)$ vs (M_H) with ANN, AE vs (M_H) and (e) curve fitting for $f'(\eta)$ vs (M_H).

Figures 4a to 4e depict the LMS-NNA design influence of Grashof number (Gr) on $f'(\eta)$, accompanied by the analysis of curve fitting. As (Gr) intensifies the augmentation in $f'(\eta)$ is observed for both mono and hybrid nanofluids as depicted in Figs. 4a and 4c. As (Gr) increases, indicating a greater influence of buoyancy forces relative to viscous forces in the fluid flow, there is a notable augmentation observed in the velocity distribution. This phenomenon can be interpreted physically in the context of buoyancy-driven fluid dynamics. With the growth in (Gr), buoyancy forces become increasingly dominant, leading to enhanced fluid motion and convective heat transfer. Consequently, the velocity distribution $f'(\eta)$ experiences a rise, with fluid particles accelerating to higher velocities as they respond to the intensified buoyancy-driven flow. This augmentation in velocity distribution reflects the increased convective transport of momentum within the fluid, resulting in more vigorous fluid motion and alterations in flow patterns. The error analysis associated with velocity profiles against variations in (Gr) is depicted in Figs. 4b and 4d. In fluid dynamics, error analysis constitutes a crucial step in assessing the reliability and accuracy of predictive models. In our model, absolute error values are meticulously examined, with these values falling within range 10^{-7} to 10^{-3} corresponding to the configurations of their respective artificial neural networks (ANNs). These numerical findings serve as a vital metric for gauging the performance of the models. When juxtaposed with reference outputs obtained from theoretical data, the error analysis confirms the commendable level of accuracy within the specified range given by 10^{-7} to 10^{-3}, thus validating the efficacy of the designed ANN models. Figure 4e depicts the curve fitting for (Gr) against $f'(\eta)$.
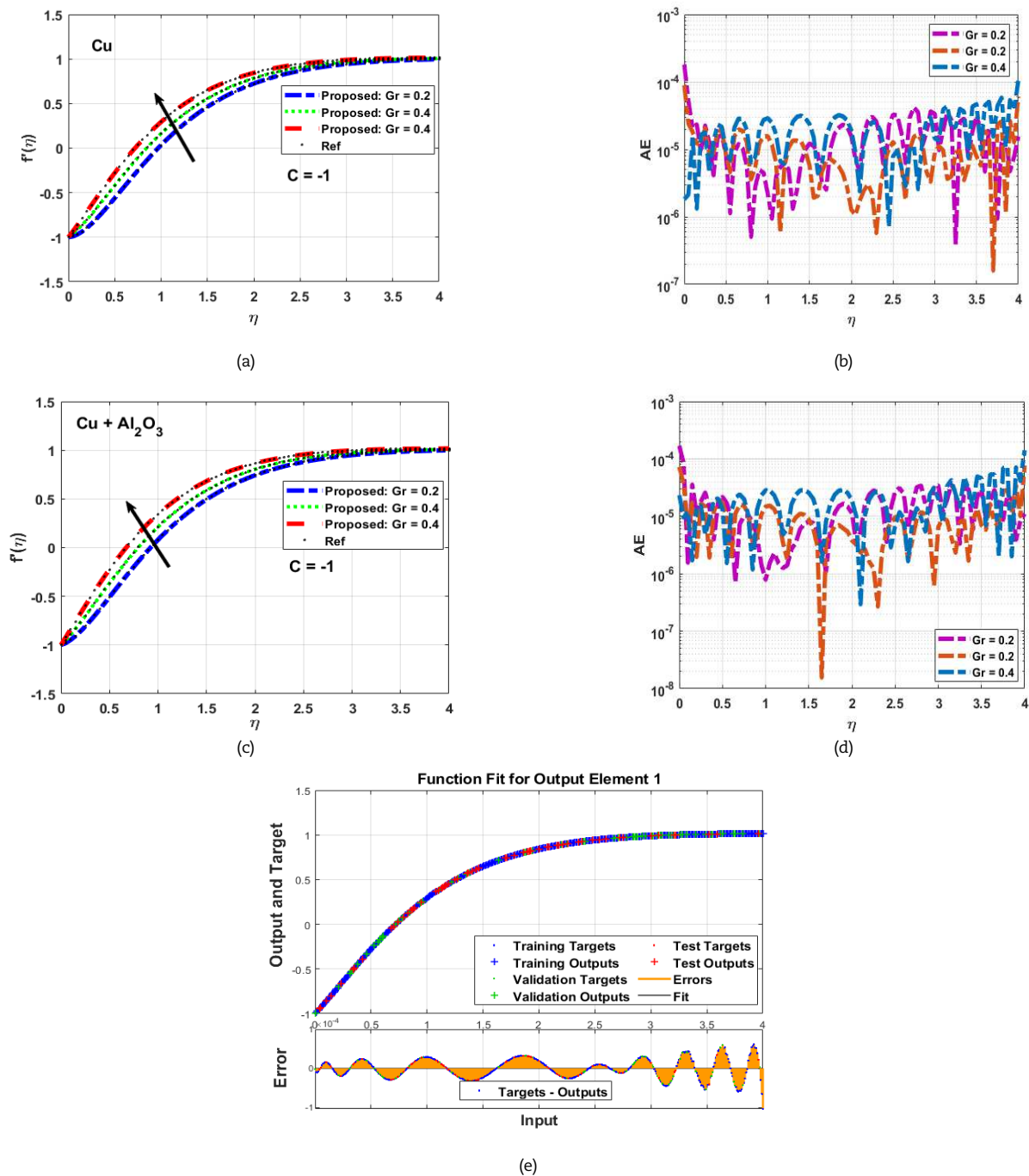

(a)

(b)

(c)

(d)

(e)

Fig. 4. Impacts of Gr on $f'(\eta)$ with curve fitting analysis: (a) behavior of $f'(\eta)$ vs Gr with ANN, (b) AE vs Gr, (c) behavior of $f'(\eta)$ vs Gr with ANN, (d) AE vs Gr, (e) curve fitting for $f'(\eta)$ vs Gr.

Figures 5a to 5e display the impact of Casson factor (β) on $f'(\eta)$. As (β) escalates, there is a noticeable hindrance in $f'(\eta)$, as depicted in Fig. 5a. The observed reduction in $f'(\eta)$ in both mono and hybrid nanofluid scenarios as (β) increases can be attributed to the rheological properties of the fluid. Clearly, represents the fluid's resistance to flow, and as it grows, the fluid becomes more viscous and less able to flow freely. This increased viscosity impedes the movement of the fluid particles, resulting in a decrease in velocity distribution as depicted in Fig. 5a. In the context of hybrid nanofluids, the presence of nanoparticles can further amplify this effect by introducing additional resistance to flow and reduced further $f'(\eta)$ as portrayed in Fig. 5c. Overall, the increase in (β) signifies a transition towards more viscous behavior, leading to a reduction in $f'(\eta)$ across both mono and hybrid nanofluid systems. The error analysis associated with velocity profiles against variations in (β) is depicted in Figs. 5b and 5d. In fluid dynamics, error analysis constitutes a crucial step in assessing the reliability and accuracy of predictive models. Fig. 5e centers on curve fitting analysis, for variations in (β) against velocity curves. In this context, it helps understand how well the mathematical model aligns with observed velocity profiles with changing (β).
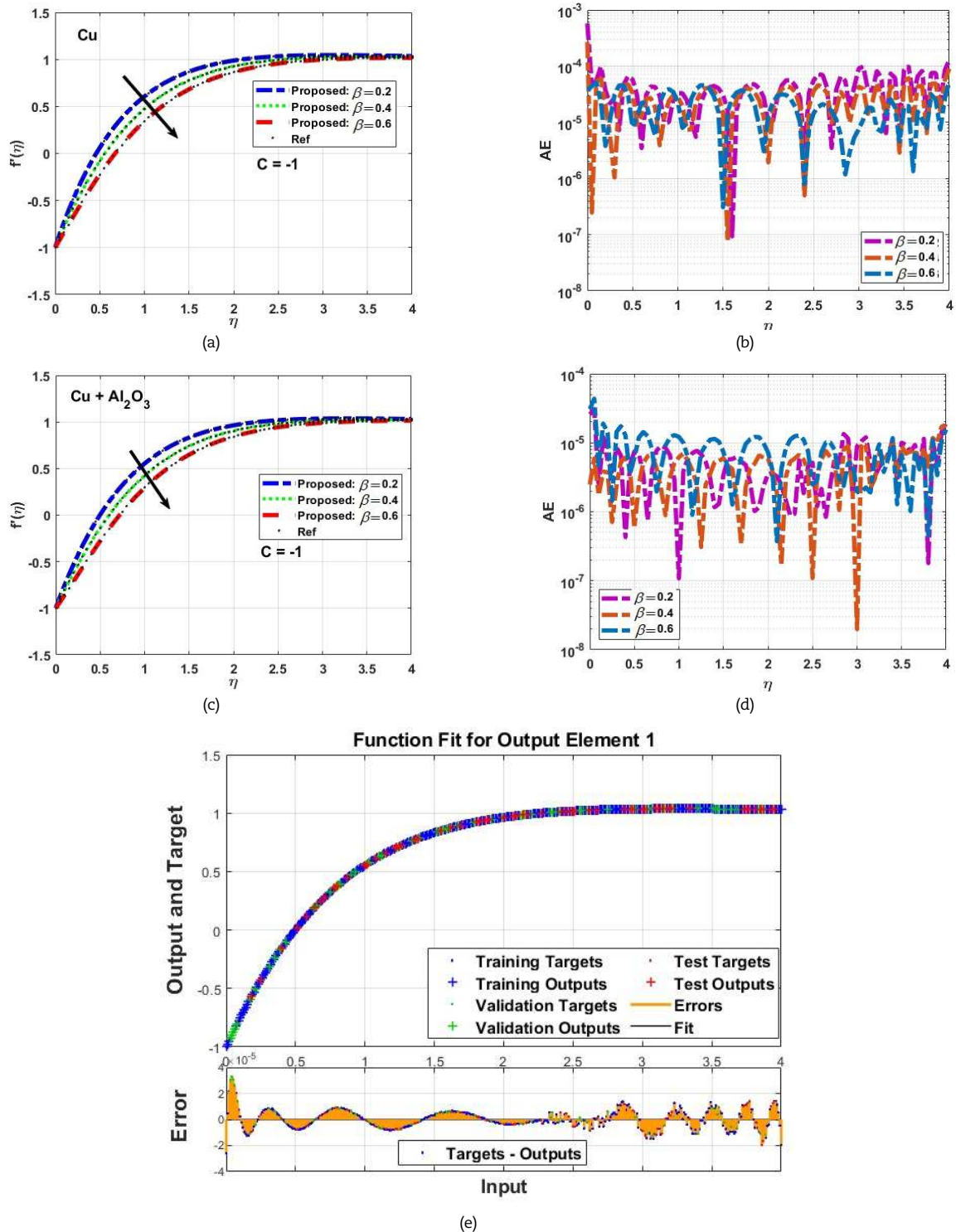

Fig. 5. Impacts of β on $f'(\eta)$ with analysis of curve fitting: (a) behavior of $f'(\eta)$ vs β with ANN, (b) AE vs β, (c) behavior of $f'(\eta)$ vs β with ANN, (d) AE vs β, (e) curve fitting for $f'(\eta)$ vs β.

Figures 6a to 6e illustrate how the Eckert number (*Ec*) affects $\Theta(\eta)$ in both nanofluid and hybrid nanofluid scenarios. Actually, (*Ec*) plays a crucial role in determining $\Theta(\eta)$ within nanofluid flow, representing the relationship amid kinetic and internal energies, as depicted in Fig. 6a. With growth in (*Ec*) kinetic energy has more dominance over internal energy that ultimately enhanced the width of thermally layer at boundary and supports the thermal panels as portrayed in Fig. 6a. It is also obvious that $\Theta(\eta)$ is rising for both the scenarios (*Ec* < 0 & *Ec* > 0), i.e. *Ec* = -3.0, -5.0, -7.0 and *Ec* = 3.0, 5.0, 7.0. For these values an analogous behavior has noticed for hybrid nanofluid flow as depicted in Fig. 6c. On the domains *Ec* = -3.0, -5.0, -7.0 and *Ec* = 3.0, 5.0, 7.0, an error analysis has portrayed in Figs. 6b and 6d, while the curve fitting is analyzed in Fig. 6e.
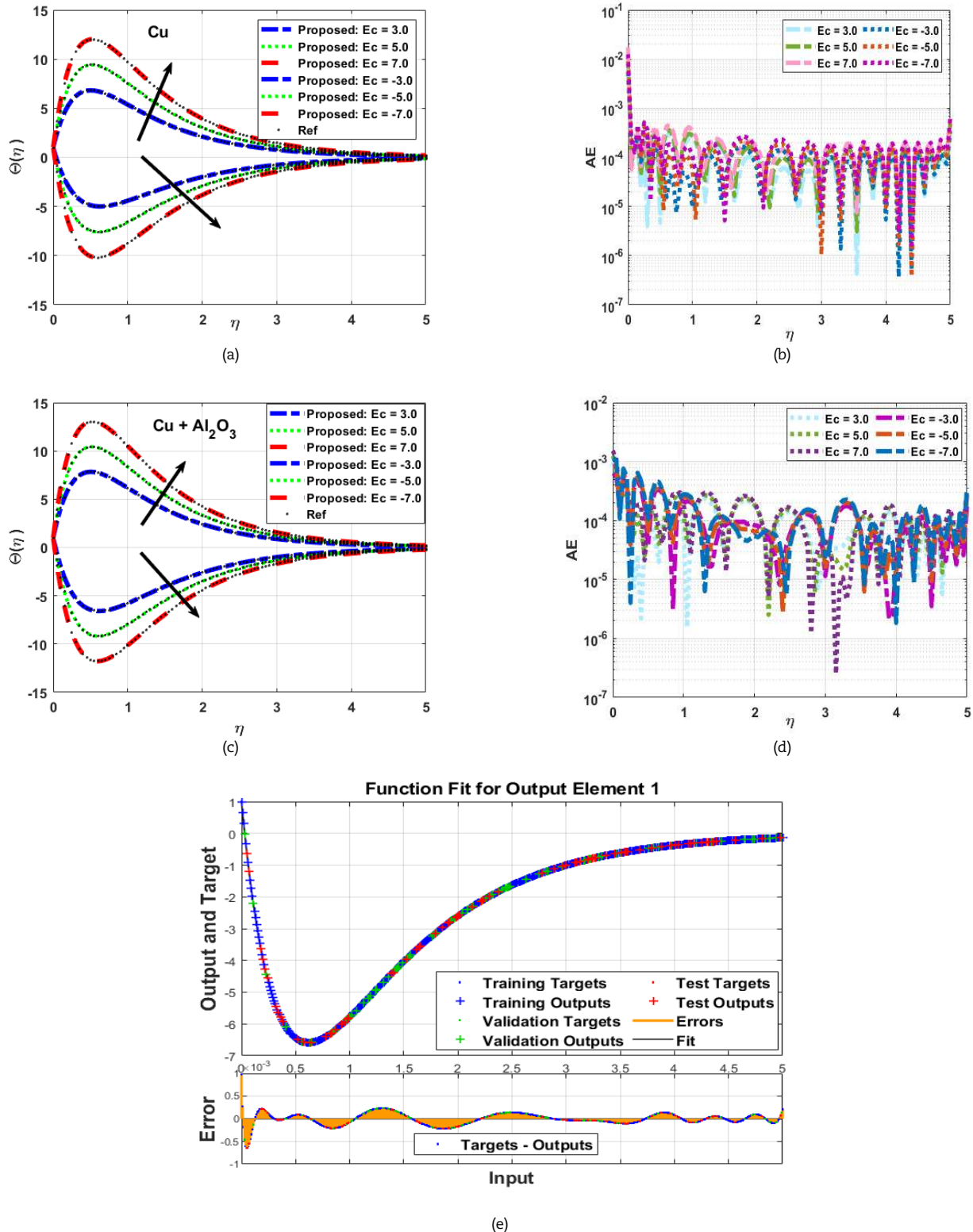

(a)

(b)

(c)

(d)

(e)

Fig. 6. Impact of *Ec* vs $\Theta(\eta)$ with curve fitting analysis: (a) behavior of $\Theta(\eta)$ vs *Ec* with ANN, (b) AE vs *Ec*, (c) behavior of $\Theta(\eta)$ vs *Ec* with ANN, (d) AE vs *Ec*, (e) curve fitting for $\Theta(\eta)$ vs *Ec*.

Figures 7a to 7e portray the influence of radiation factor (Rd) on $\Theta(\eta)$ regarding mono and hybrid nanofluids. Growth in (Rd) causes upsurge in $\Theta(\eta)$ as depicted in Figs. 7a and 7c. The observed phenomenon can be elucidated by the escalating importance of radiative heat transfer, particularly in response to the thermal characteristics of nanoparticles. As (Rd) intensifies, it indicates a larger influence of radiative heat transfer mechanisms within the nanofluid system. This heightened radiation factor prompts an elevation in temperatures throughout the system, influencing the thermal behavior and overall heat transfer dynamics. In nanofluid systems containing nanoparticles or hybrid nanoparticles, the presence of these nanoscale materials significantly modifies the thermal conductance and emissivity properties, amplifying the role of radiative heat transfer. Consequently, as the radiation factor increases, a larger proportion of heat transfer occurs through radiation, leading to raised thermal flow of fluid. Figures 7b and 7d depict error analysis for mono and hybrid nanoparticles, whereas Fig. 7e depicts curve fitting that demonstrates how the model's accuracy and reliability have been ensured in the presented scenario.
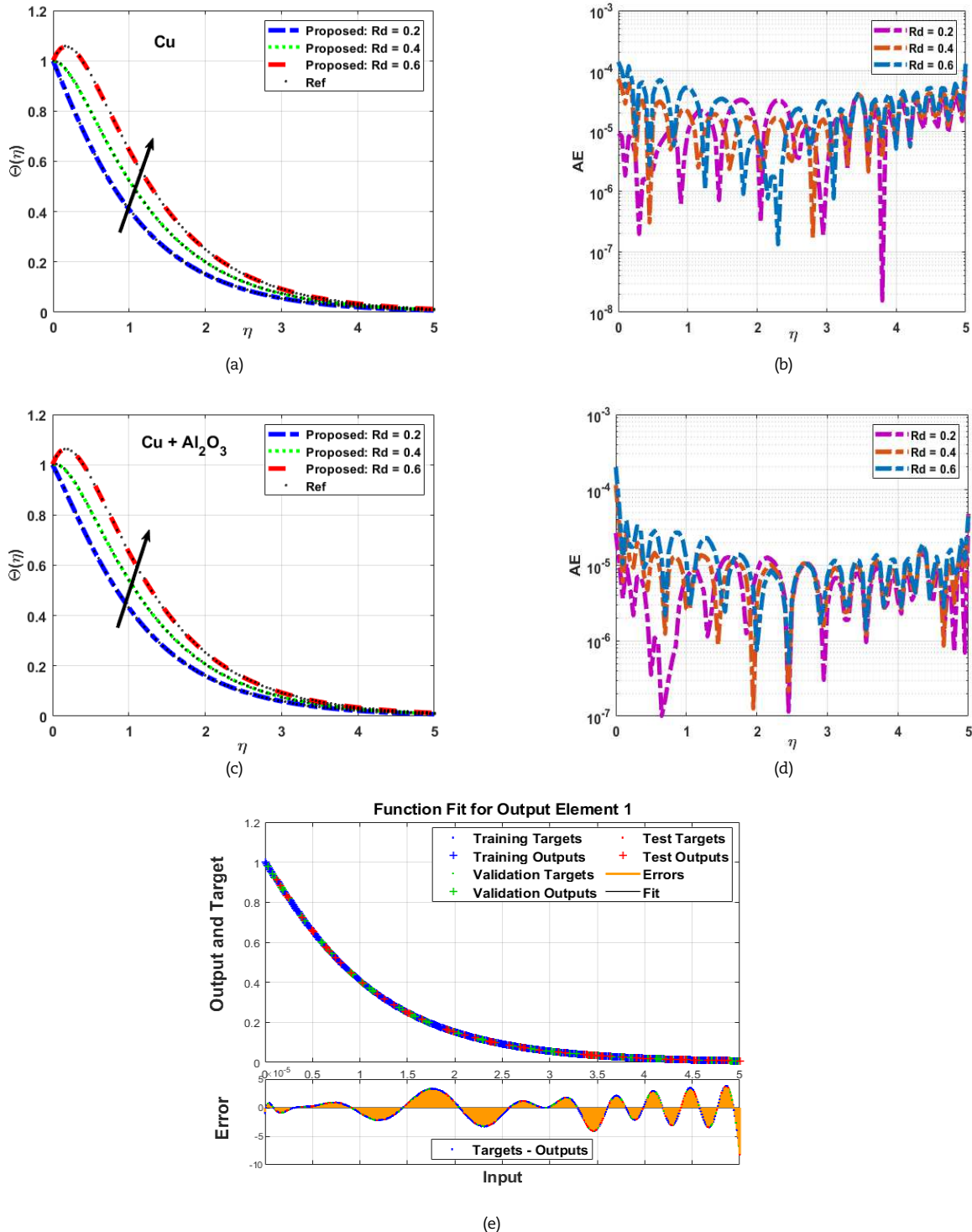

(a)

(b)

(c)

(d)

(e)

Fig. 7. Influence of Rd vs $\Theta(\eta)$ with analysis of curve fitting: (a) behavior of $\Theta(\eta)$ vs Rd with ANN, (b) AE vs Rd, (c) behavior of $\Theta(\eta)$ vs Rd with ANN, (d) AE vs Rd, (e) curve fitting for $\Theta(\eta)$ vs Rd.

The influence of nanoparticles concentrations (ϕ_1, ϕ_2) on $\Theta(\eta)$ is depicted in Figs. 8a to 8e for mono and hybrid nanoparticles with an augmenting behavior of $\Theta(\eta)$ against growth in values of nanoparticle number. The augmentation in thermal profiles observed with the increasing concentration of nanoparticles in both nanofluid and hybrid nanofluid systems can be attributed to enhanced heat transfer mechanisms facilitated by the presence of nanoparticles. As the nanoparticle concentration grows, so does the density of heat transfer sites within the fluid, leading to more efficient conduction, convection, and radiation processes. The nanoparticles act as effective conduits for thermal energy, facilitating the transfer of heat across the fluid medium. Additionally, their high surface area-to-volume ratios enhance convective heat transfer by promoting better mixing and fluid dispersion. Furthermore, in hybrid nanofluids, the combination of different nanoparticle types can synergistically improve thermal conductivity and heat transfer characteristics, further augmenting the thermal profiles. An error analysis is provided in Figs. 8b and 8d for both nanoparticles and hybrid nanoparticles. Additionally, in Fig. 8e, curve fitting is presented to demonstrate how the accuracy and reliability of the model have been ensured in the scenario.
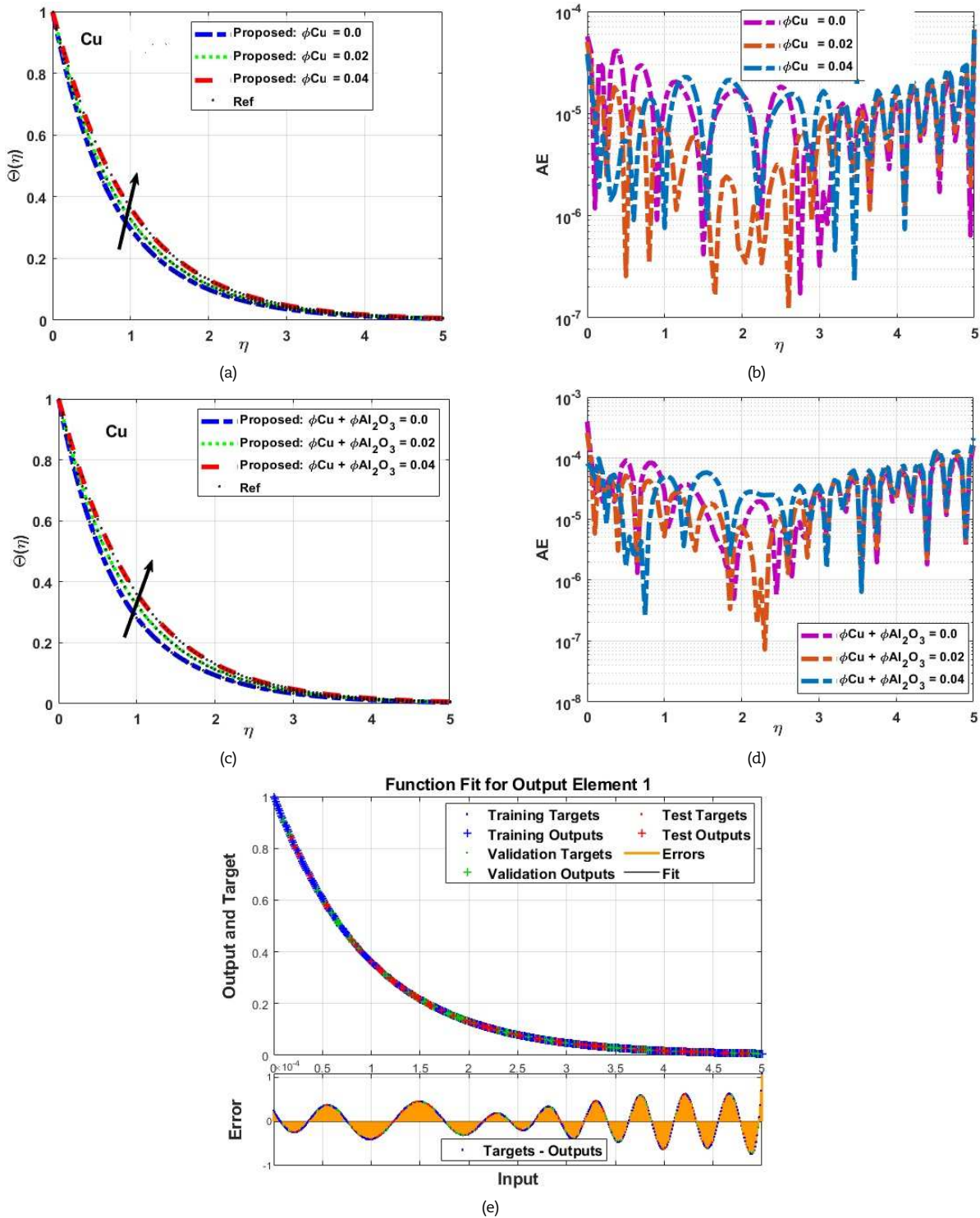

Fig. 8. Impact of ϕ_1, ϕ_2 vs $\Theta(\eta)$ with curve fitting analysis: (a) behavior of $\Theta(\eta)$ vs ϕ_1, ϕ_2 with ANN, (b) AE vs ϕ_1, ϕ_2, (c) behavior of $\Theta(\eta)$ vs ϕ_1, ϕ_2 with ANN, (d) AE vs ϕ_1, ϕ_2, (e) curve fitting for $\Theta(\eta)$ vs ϕ_1, ϕ_2.

The influence of unsteadiness factor (S) on $\Theta(\eta)$ is depicted in Figs. 9a to 9e for mono and hybrid nanoparticles. With upsurge in (S) there is reduction in $\Theta(\eta)$ as shown in Figs. 9a and 9c. The reduction in thermal profiles observed with the increasing unsteadiness factor in both nanofluid and hybrid nanofluid systems can be attributed to the destabilizing effect of unsteady flow conditions on heat transfer processes. As (S) grows, it signifies a greater degree of flow fluctuation as well as temporal variation within the fluid medium. This increased flow instability disrupts the orderly transfer of thermal energy, leading to a reduction in thermal profiles. The fluctuations in flow velocity and temperature gradients hinder the establishment of thermal equilibrium and diminish the effectiveness of heat transfer mechanisms such as conduction, convection, and radiation. Consequently, the thermal profiles exhibit a decrease as the unsteadiness factor intensifies, reflecting the disruptive influence of unsteady flow dynamics on the thermal behavior of nanofluid and hybrid nanofluid systems. The error analysis depicted in Figs. 9b and 9d offers a quantitative evaluation of the model's accuracy in catching these fluctuations. The absolute error values computed in our model fall within 10^{-7} to 10^{-3} specific to their corresponding ANN configurations. Figure 9e depicts the analysis of curve fitting for variations in (S).
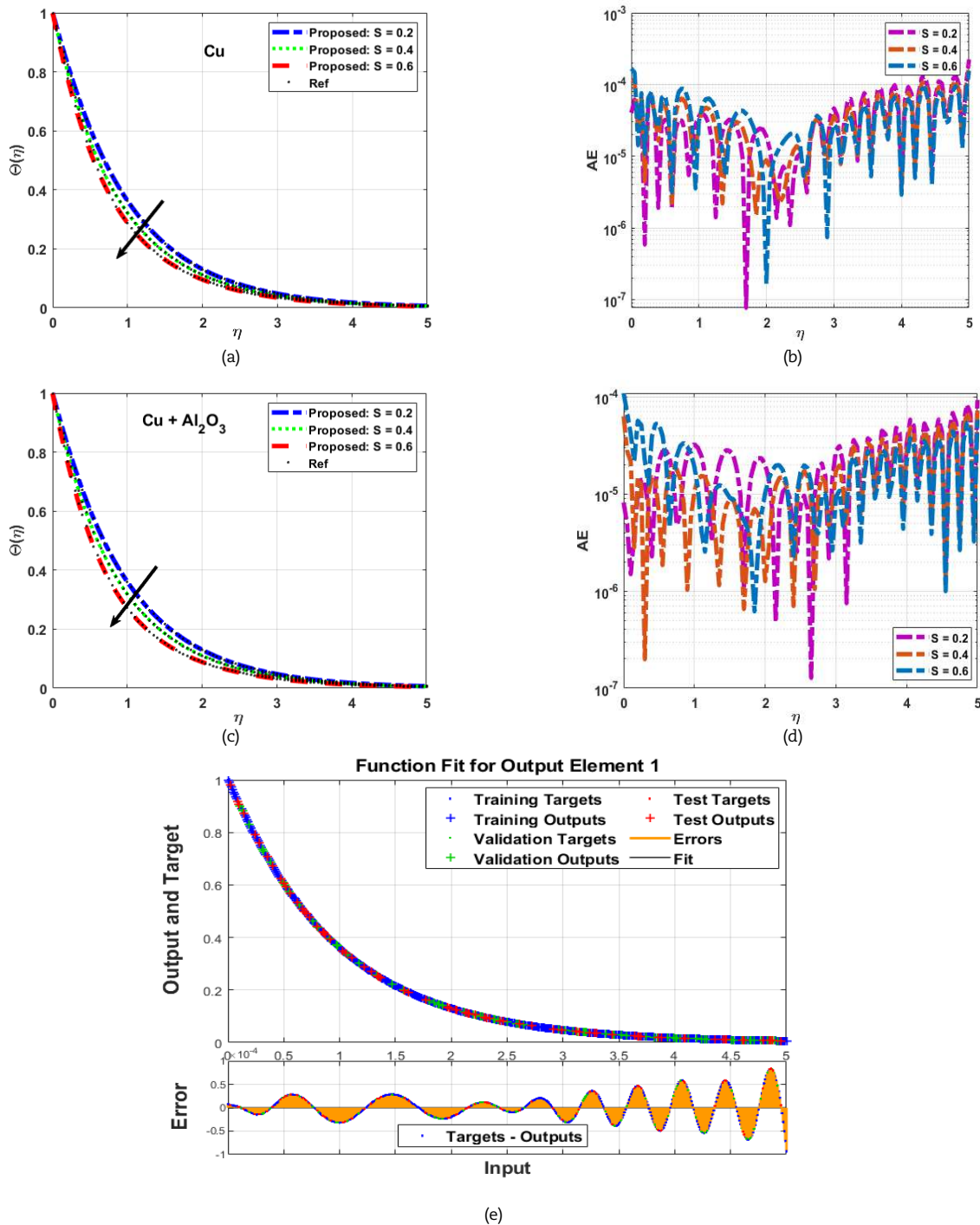

(a)

(b)

(c)

(d)

(e)

Fig. 9. Impacts of S vs $\Theta(\eta)$ using curve fitting analysis: (a) behavior of $\Theta(\eta)$ vs S with ANN, (b) AE vs S, (c) behavior of $\Theta(\eta)$ vs S with ANN, (d) AE vs S, (e) curve fitting for $\Theta(\eta)$ vs S.

The impacts of radiation factor (Rd) on generation of entropy ($S_G(\eta)$) are depicted in Figs. 10a to 10c. In Fig. 10a, the impacts of (Rd) on ($S_G(\eta)$) have noticed. The increase in (Rd) has led to a notable rise in entropy generation, particularly pronounced in hybrid nanoparticles compared to nanofluids. Physically, (Rd) enhancement implies greater absorption and emission of thermal radiation within the system, intensifying energy transfer processes. In the case of hybrid nanoparticles, which typically possess diverse material compositions and structures, this heightened radiation absorption results in more complex energy dissipation pathways, leading to increased entropy generation. Moreover, the hybrid nature of these nanoparticles facilitates synergistic effects between fluid's particles, further enhancing entropy generation. An error analysis is detailed in Fig. 10b for nanoparticles and hybrid nanoparticles. Meanwhile, Fig. 10c presents curve fitting, demonstrating how the exactness and consistency of model are ensured.

The influence of radiative factor (Rd) on Bejan Number ($Be(\eta)$) is depicted in Figs. 11a to 11c. In Fig. 11a, the impacts of (Rd) on ($Be(\eta)$) have noticed with an upsurge in ($Be(\eta)$) against growth in (Rd). The increase in radiation factor leading to augmentation in the Bijan number signifies a heightened level of radiative heat transfer relative to convective heat transfer within a system. The Bijan number compares the relative significance of radiation and convection in heat transfer processes. As radiation becomes more dominant, the Bijan number increases, indicating that radiative heat transfer plays a more substantial role compared to convective heat transfer. This augmentation implies that the system experiences a greater influence of electromagnetic radiation in transferring thermal energy, which could have significant implications for temperature distribution, energy transfer rates, and overall heat transfer characteristics within the system. Such insights have many applications including engineering and industry. The error is analyzed in Fig. 11b for both nanoparticles and hybrid nanoparticles. Additionally, Fig. 11c illustrates curve fitting, showcasing how the model's accuracy and reliability are upheld.
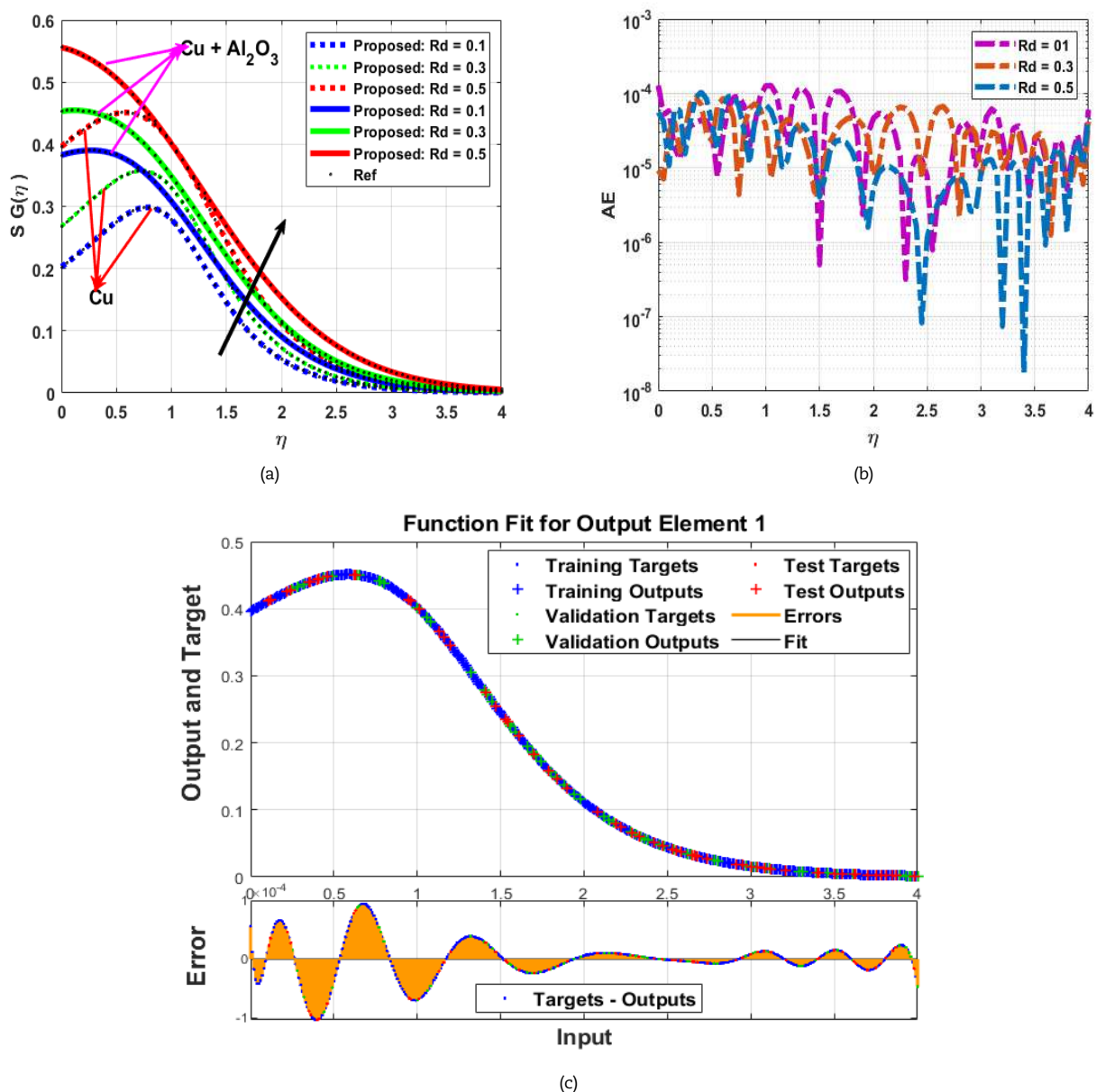

(a)

(b)

(c)

Fig. 10. Impacts of Rd on $S_G(\eta)$ with curve fitting analysis: (a) behavior of $S_G(\eta)$ vs Rd with ANN, (b) AE vs Rd, (c) curve fitting for $S_G(\eta)$ vs Rd.

The impacts of Brinkman number (Br) on generation of entropy ($S_G(\eta)$) are depicted in Figs. 12a to 12c. In Fig. 12a, the impacts of (Br) on ($S_G(\eta)$) have noticed. The increase in (Br) has led to a notable rise in entropy generation, particularly pronounced in hybrid nanoparticles compared to nanofluids. This phenomenon is particularly pronounced when comparing hybrid nanoparticles to nanofluids. The augmentation in (Br) indicates a stronger influence of viscous forces, altering the fluid dynamics and consequently impacting ($S_G(\eta)$). In the context of hybrid nanoparticles and nanofluids, the presence of nanoparticles enhances the interactions within the fluid, leading to intensified viscous dissipation and consequently increased entropy generation. This heightened entropy generation underscores the complexity of fluid flow behavior in these systems and highlights the importance of considering nanoparticle characteristics in predicting and understanding entropy generation phenomena. Figure 12b illustrates an error analysis for mono and hybrid nanoparticles. This analysis portrays how inaccuracies are depicted and assessed within the model. Additionally, Fig. 12c presents curve fitting, demonstrating how the model's accuracy and reliability are confirmed through its ability to fit data points within a specified scenario.

The impacts of Brinkman number (Br) on Bijan number ($Be(\eta)$) are depicted in Figs. 13a to 13c. In Fig. 13a, the impacts of (Br) on ($Be(\eta)$) have noticed. The increase in (Br) has led to a notable rise in ($Be(\eta)$) particularly pronounced in hybrid nanoparticles compared to nanofluids. Physically interpreting this, as (Br) increases, it indicates a heightened impact of viscous forces on fluid flow. The decrease in (Br), implies that thermal diffusion is reserved compared to viscous diffusion. The analysis of error is depicted in Fig. 13b for both mono and hybrid nanoparticles. Meanwhile, Fig. 13c illustrates curve fitting, demonstrating how the model's accuracy and reliability are ensured within a specific scenario.
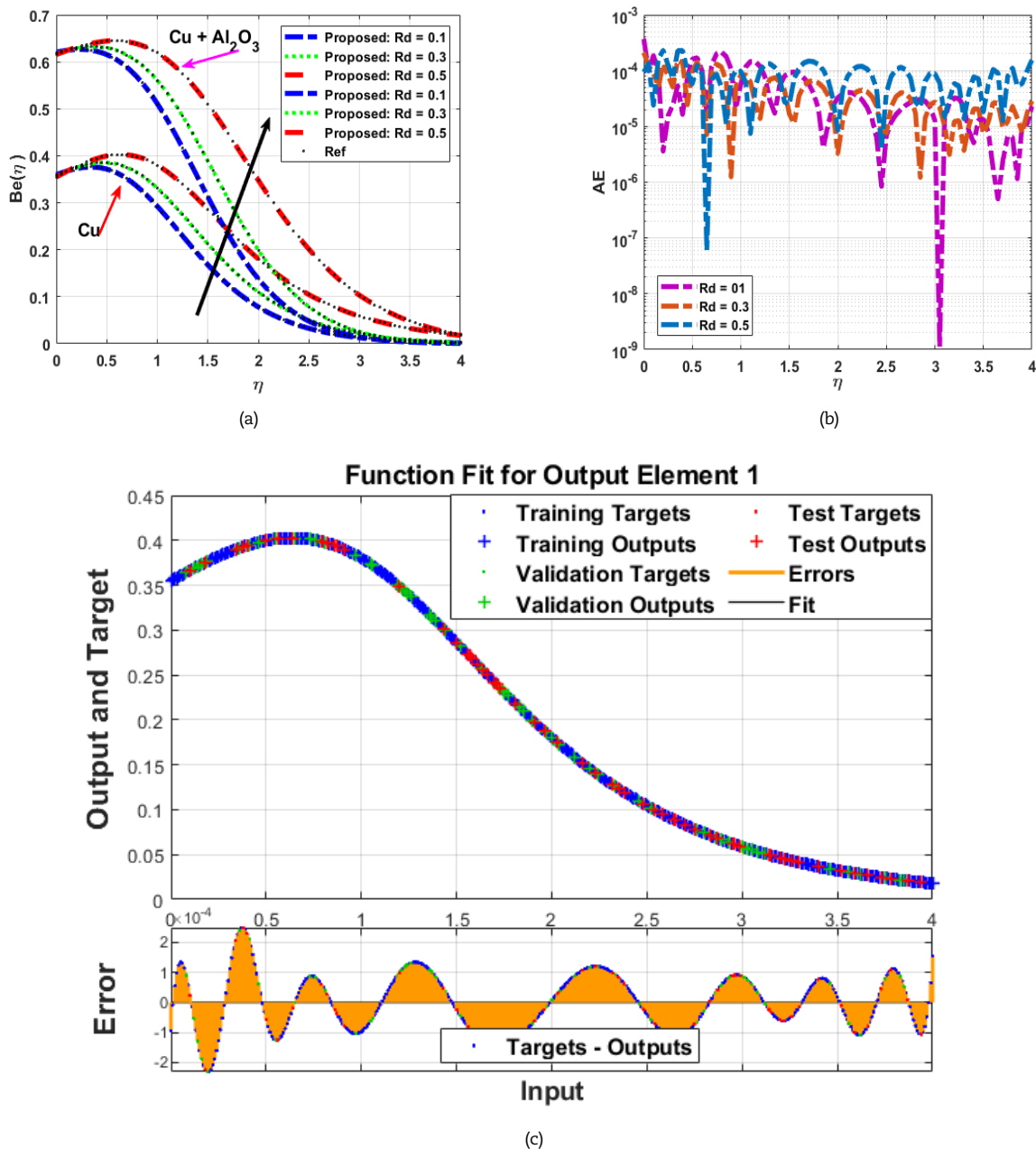

(a)

(b)

(c)

Fig. 11. Effects of Rd vs $Be(\eta)$ with analysis of curve fitting: (a) behavior of $Be(\eta)$ vs Rd with ANN, (b) AE vs Rd, (c) curve fitting for $Be(\eta)$ vs Rd.
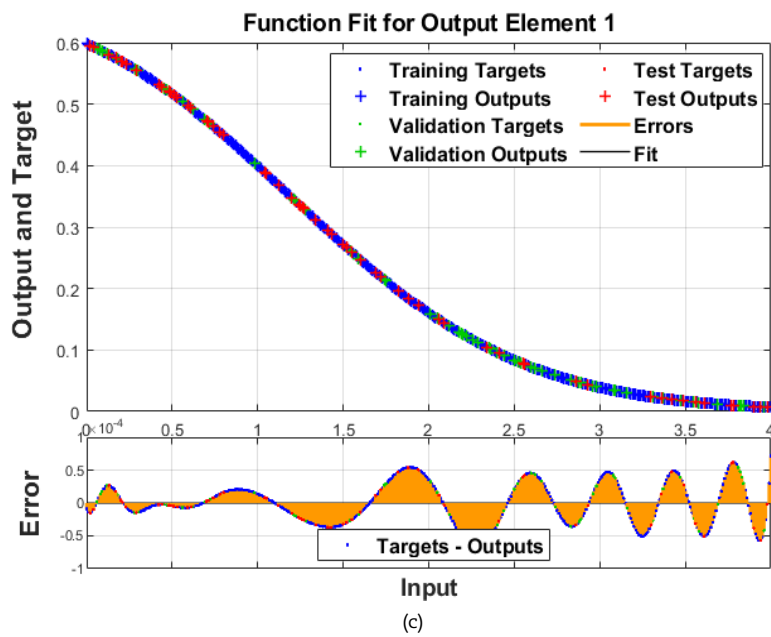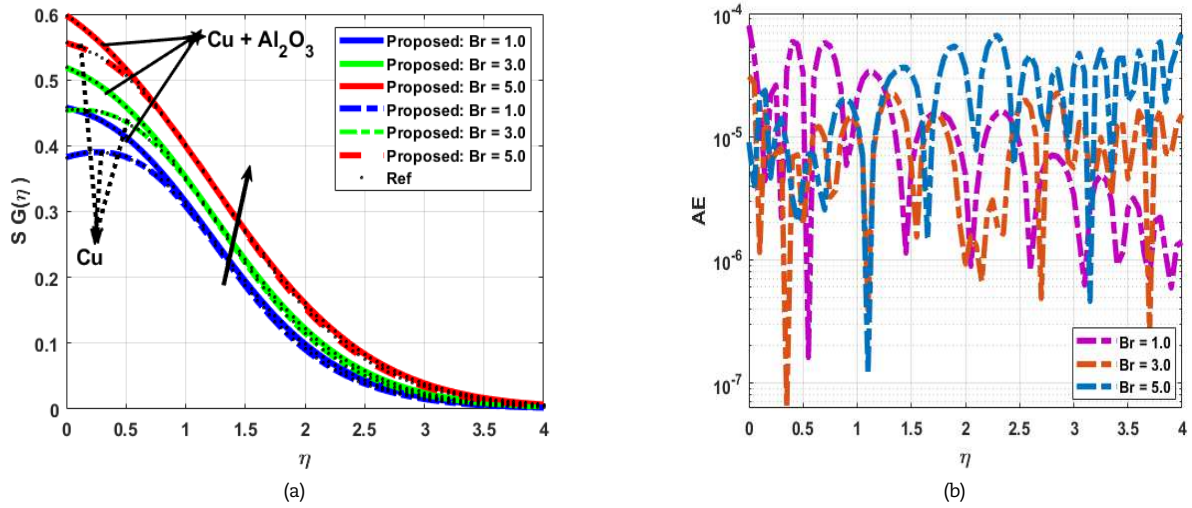
Fig. 12. Impacts of Br on $S_G(\eta)$ with analysis of curve fitting: (a) behavior of $S_G(\eta)$ vs Br with ANN, (b) AE vs Br, (c) curve fitting $S_G(\eta)$ vs Br.
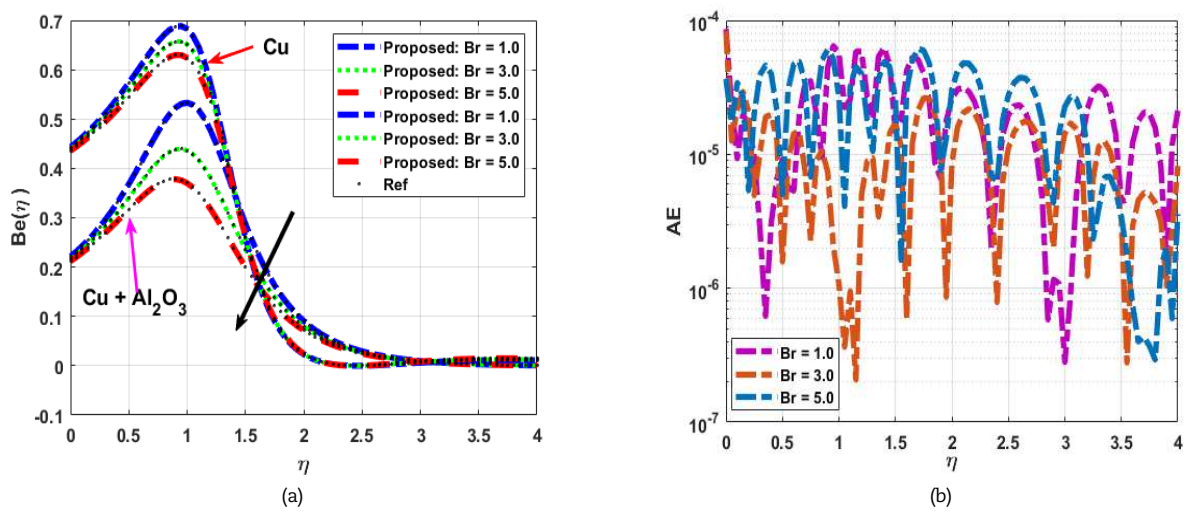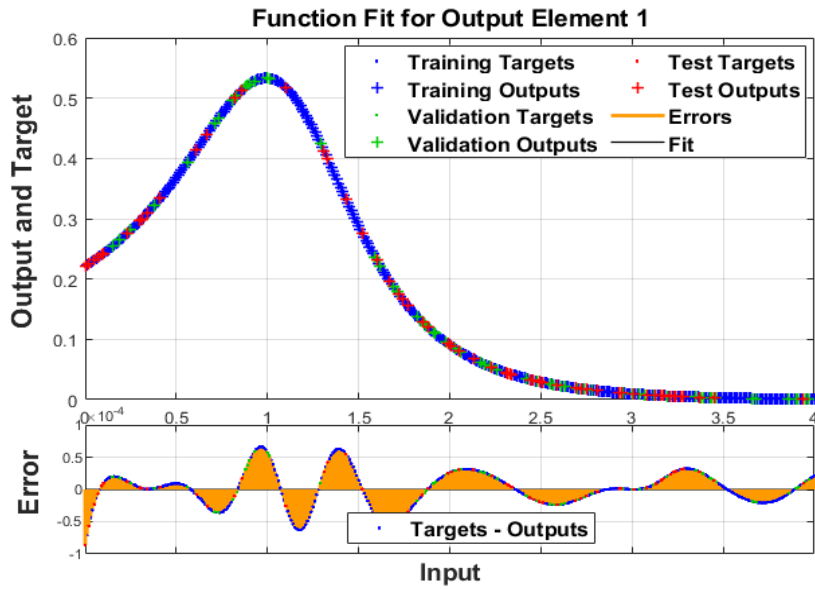

Fig. 13. Effects of Br on $Be(\eta)$ with analysis of curve fitting: (a) behavior of $Be(\eta)$ vs Br with ANN, (b) AE vs Br, (c) curve fitting for $Be(\eta)$ vs Br.

(c)

Fig. 13. Continued.

Table 2 serves as a comprehensive repository of numerical data crucial to the Artificial Neural Network (ANN) approach. This table encompasses key stages of training, validation, and testing, all evaluated using Mean Squared Error (MSE). Additionally, the table provides insights into the gradient, performance, and mu parameter associated with different epochs, offering a holistic view of the model's behavior over time. The dataset in Table 2 includes an analysis of velocity performance in response to variations in different factors at epochs 780, 342, and 85. This data sheds light on how the model's velocity predictions change as the input factors vary, offering valuable insights into the sensitivity of the model to different inputs. Furthermore, the table presents thermal flow performance against variations in emerging factors at epochs 990, 548, 350, and 300. This analysis highlights how the model performs in predicting thermal flow under changing conditions, providing important information for optimizing the model's accuracy and performance. Additionally, Table 2 evaluates entropy generation at epochs 200 and 90, providing insights into the system's disorder or randomness. The table also examines the Bejan number at epochs 250 and 780, which is crucial for understanding the balance between convection and diffusion in the system. Overall, Table 1 offers a detailed and multifaceted view of the ANN model's performance and behavior across various factors and epochs. The results of current work have been compared in Table 3 with already available data in the literature and a fine agreement has been ensured among all the dataset.

Table 2. Results for various scenarios regarding mono and hybrid nanoparticles flow.

Cases	MSE			Performance	Gradient	Mu	Epoch	Time (s)
	Training	Validation	Testing					
Performance of velocity across different factors								
M_H	2.74010×10^{-10}	4.54366×10^{-10}	2.66543×10^{-10}	3.25×10^{-10}	8.57×10^{-8}	1.0×10^{-9}	780	02
Gr	2.98767×10^{-10}	5.6643×10^{-10}	3.5643×10^{-10}	4.89×10^{-10}	8.76×10^{-8}	1.0×10^{-8}	342	03
Λ	4.2565×10^{-11}	1.2765×10^{-10}	6.3452×10^{-11}	6.34×10^{-11}	6.45×10^{-7}	1.0×10^{-9}	85	01
Performance of thermal flow across different factors								
Ec	4.0023×10^{-8}	3.2431×10^{-8}	4.4252×10^{-8}	4.11×10^{-8}	5.11×10^{-5}	1.0×10^{-7}	990	07
Rd	7.1102×10^{-10}	9.5643×10^{-10}	8.8976×10^{-10}	7.01×10^{-10}	9.54×10^{-8}	1.0×10^{-8}	548	05
ϕ_1, ϕ_2	7.9906×10^{-10}	7.5708×10^{-10}	8.2636×10^{-10}	7.99×10^{-10}	9.92×10^{-8}	1.0×10^{-8}	300	02
S	5.7367×10^{-10}	7.9196×10^{-10}	7.8932×10^{-10}	5.74×10^{-10}	9.95×10^{-8}	1.0×10^{-8}	340	01
Generation of entropy across different factors								
Rd	2.4325×10^{-9}	2.7654×10^{-9}	2.9181×10^{-9}	2.10×10^{-9}	9.88×10^{-8}	1.0×10^{-9}	200	02
Be	7.9876×10^{-10}	7.9876×10^{-10}	7.9196×10^{-10}	5.74×10^{-10}	9.92×10^{-8}	1.0×10^{-9}	90	01
Bejan number across different factors								
Rd	6.8765×10^{-9}	7.7654×10^{-9}	8.7865×10^{-9}	7.44×10^{-9}	1.0×10^{-7}	1.0×10^{-8}	250	02
Be	2.1432×10^{-9}	1.7654×10^{-9}	2.8765×10^{-10}	1.55×10^{-9}	9.95×10^{-8}	1.0×10^{-9}	780	04

Table 3. Comparison of current findings with dataset in existing literature [42, 49].

	Lok and Pop [42]	Ishak et al. [49]	Current Data
$c = b / \alpha$	$R_e^{0.5}Cf$	$R_e^{0.5}Cf$	$R_e^{0.5}Cf$
-1.5	0.353782981360	0.34527832000	0.3565271878200
-1.2	0.532789016670	0.52671589290	0.5335627827890
-1.0	1.132789166300	1.12499156270	1.1332678127890

6. Conclusions

This study examined the generation of irreversibility and the behavior of stagnation point hybrid nanofluid flow on a Riga plate. The effects of nonlinear thermal convection and solar radiation were incorporated in flow problem. The nanoparticles of (Cu) and (Al_2O_3) were mixed with Glycol ($C_3H_8O_2$) to obtain hybrid nanofluid. The main equations are converted to dimensionless forms using a set of suitable variables and were then solved by employing ANN. After in-depth examination, the following points have been deduced:

- An increase in the Grashof number and EMHD Riga plate factor leads to heightened velocity panels for mono and hybrid nanoparticles.
- The expansion of the width factor of magnet/electrode results in a decrease in velocity distribution.
- Higher Eckert numbers in both scenarios ($Ec > 0$) and ($Ec < 0$) contribute to an acceleration in thermal panels.
- Increased radiative factor and nanoparticles concentration support the rise in thermal panels, while an increase in unsteadiness factor retards heat flow for both mono and hybrid nanoparticles.
- Entropy generation and Bejan number exhibit escalating trends with the radiation factor, with a more pronounced impact observed in hybrid nanoparticles.
- The Brinkman number positively influences entropy generation but retards Bejan number behavior.
- Graphical curve fitting by employing LMS-NNA within ANNs effectively showcases the model's approximation of input-output relationships, aiding in understanding its performance in capturing underlying data patterns.
- The analysis of absolute error, conducted for the influences of physical factors on velocity and thermal distributions, entropy generation, and Bejan number, ensures great correctness in ANN models.
- In future work, the Riga plate will be placed in inclined position and its impact will be incorporated in the proposed model. Moreover, the impacts of Buongiorno model will also be included in it.

Authors Contribution

A. Khan, A. Mouldi, T. Gul & H. Ayed: Solution and writing manuscript; T. Gul, H.A. El-Wahed Khalifa: Software; A.M. Alanzi, T. Gul, A. Khan: Validation. The manuscript was written through the contribution of all authors. All authors discussed the results, reviewed, and approved the final version of the manuscript.

Acknowledgments

Funding

Conflicts of Interest

The authors declare no conflict of interest.

Data Availability Statement

The datasets generated and/or analyzed during the current study are available from the corresponding author on reasonable request.

References

[1] Choi, S.U.S., *Enhancing thermal conductivity of fluids with nanoparticles*, in: D.A. Siginer, H.P. Wang (Eds.), Developments and Applications of Non-Newtonian Flows, FED, ASME, New York, 99-105, 1995.

[2] Shah, Z., Khan, A., Khan, W., Alam, M.K., Islam, S., Kumam, P., Thounthong, P., Micropolar gold blood nanofluid flow and radiative heat transfer between permeable channels, *Computer Methods and Programs in Biomedicine*, 186, 2020, 105197.

[3] Hashemi-Tilehnoee, M., Seyyedi, S.M., del Barrio, E.P., Sharifpur, M., Analysis of natural convection and the generation of entropy within an enclosure filled with nanofluid-packed structured pebble beds subjected to an external magnetic field and thermal radiation, *Journal of Energy Storage*, 73, 2023, 109223.

[4] Seyyedi, S.M., Hashemi-Tilehnoee, M., Palomo del Barrio, E., Dogonchi, A.S., Ghadami, S.M., Sharifpur, M., Electro-enhanced natural convection analysis for an Al2O3-water-filled enclosure by considering the effect of thermal radiation, *Numerical Heat Transfer, Part A: Applications*, 2023, 1-20.

[5] Islam, S., Khan, A., Kumam, P., Alrabaiah, H., Shah, Z., Khan, W., Jawad, M., Radiative mixed convection flow of maxwell nanofluid over a stretching cylinder with joule heating and heat source/sink effects, *Scientific Reports*, 10(1), 2020, 17823.

[6] Acharya, N., Mabood, F., Shahzad, S.A., Badruddin, I.A., Hydrothermal variations of radiative nanofluid flow by the influence of nanoparticles diameter and nanolayer, *International Communications in Heat and Mass Transfer*, 130, 2022, 105781.

[7] Dogonchi, AS., Chamkha, A.J., Hashemi-Tilehnoee, M., Seyyedi, S.M., Ganji, D.D., Effects of homogeneous-heterogeneous reactions and thermal radiation on magneto-hydrodynamic Cu-water nanofluid flow over an expanding flat plate with non-uniform heat source, *Journal of Central South University*, 5(26), 2019, 1161-1171.

[8] Abbasi, A., Farooq, W., Tag-ElDin, E.S.M., Khan, S.U., Khan, M.I., Guedri, K., Galal, A.M., Heat transport exploration for hybrid nanoparticle (Cu, Fe3O4)—Based blood flow via tapered complex wavy curved channel with slip features, *Micromachines*, 13(9), 2022, 1415.

[9] Eid, M.R., Nafe, M.A., Thermal conductivity variation and heat generation effects on magneto-hybrid nanofluid flow in a porous medium with slip condition, *Waves in Random and Complex Media*, 32(3), 2022, 1103-1127.

[10] Waqas, H., Farooq, U., Liu, D., Abid, M., Imran, M., Muhammad, T., Heat transfer analysis of hybrid nanofluid flow with thermal radiation through a stretching sheet: A comparative study, *International Communications in Heat and Mass Transfer*, 138, 2022, 106303.

[11] Bhatti, M.M., Öztop, H.F., Ellahi, R., Study of the magnetized hybrid nanofluid flow through a flat elastic surface with applications in solar energy, *Materials*, 15(21), 2022, 7507.

[12] Khan, D., Kumam, P., Watthayu, W., Khan, I., Heat transfer enhancement and entropy generation of two working fluids of MHD flow with titanium alloy nanoparticle in Darcy medium, *Journal of Thermal Analysis and Calorimetry*, 147(19), 2022, 10815-10826.

[13] Lone, S.A., Khan, A., Gul, T., Mukhtar, S., Alghamdi, W., Ali, I., Entropy generation for stagnation point dissipative hybrid nanofluid flow on a Riga plate with the influence of nonlinear convection using neural network approach, *Colloid and Polymer Science*, 2024, 1-26.

[14] Hashemi-Tilehnoee, M., Tashakor, S., Dogonchi, A.S., Seyyedi, S.M., Khaleghi, M., Entropy generation in concentric annuli of 400 kV gas-insulated transmission line, *Thermal Science and Engineering Progress*, 19, 2020, 100614.

[15] Khan, D., Kumam, P., Watthayu, W., Yassen, M.F., A novel multi fractional comparative analysis of second law analysis of MHD flow of Casson nanofluid in a porous medium with slipping and ramped wall heating, *ZAMM-Journal of Applied Mathematics and Mechanics/Zeitschrift für Angewandte Mathematik und Mechanik*, 2023, e202100424.

[16] Guedri, K., Khan, A., Gul, T., Mukhtar, S., Alghamdi, W., Yassen, M.F., Tag Eldin, E., Thermally dissipative flow and Entropy analysis for electromagnetic trihybrid nanofluid flow past a stretching surface, *ACS Omega*, 7(37), 2022, 33432-33442.

[17] Egbueri, J.C., Incorporation of information entropy theory, artificial neural network, and soft computing models in the development of integrated industrial water quality index, *Environmental Monitoring and Assessment*, 194(10), 2022, 693.

[18] Khan, D., Kumam, P., Watthayu, W., Multi-generalized slip and ramped wall temperature effect on MHD Casson fluid: second law analysis, *Journal of Thermal Analysis and Calorimetry*, 147(23), 2022, 13597-13609.

[19] Khan, D., Asogwa, K.K., Akkurt, N., Kumam, P., Watthayu, W., Sitthithakerngkiet, K., Development of generalized Fourier and Fick's law of electro-osmotic MHD flow of sodium alginate based Casson nanofluid through inclined microchannel: exact solution and entropy generation, *Scientific Reports*, 12(1), 2022, 18646.

[20] Khan, A., Shah, Z., Alzahrani, E., Islam, S., Entropy generation and thermal analysis for rotary motion of hydromagnetic Casson nanofluid past a rotating cylinder with Joule heating effect, *International Communications in Heat and Mass Transfer*, 119, 2020, 104979.

[21] Khan, A., Saeed, A., Gul, T., Mukhtar, S., Ali, I., Jawad, M., Radiative swirl motion of hydromagnetic Casson nanofluid flow over rotary cylinder using Joule dissipation impact, *Physica Scripta*, 96(4), 2021, 045206.

[22] Sharma, J., Ahammad, N.A., Wakif, A., Shah, N.A., Chung, J.D., Weera, W., Solutal effects on thermal sensitivity of casson nanofluids with comparative investigations on Newtonian (water) and non-Newtonian (blood) base liquids, *Alexandria Engineering Journal*, 71, 2023, 387-400.

[23] Bhadauria, B.S., Kumar, A., Rawat, S.K., Yaseen, M., Thermal instability of Tri-hybrid Casson nanofluid with thermal radiation saturated porous medium in different enclosures, *Chinese Journal of Physics*, 87, 2024, 710-727.

[24] Majeed, A.H., Mahmood, R., Shahzad, H., Pasha, A.A., Raizah, Z.A., Hosham, H.A., Hafeez, M.B., Heat and mass transfer characteristics in MHD Casson fluid flow over a cylinder in a wavy channel: Higher-order FEM computations, *Case Studies in Thermal Engineering*, 42, 2023, 102730.

[25] Raje, A., Koyani, F., Bhise, A.A., Ramesh, K., Heat transfer and entropy optimization for unsteady MHD Casson fluid flow through a porous cylinder: Applications in nuclear reactors, *International Journal of Modern Physics B*, 37(25), 2023, 2350293.

[26] Tijani, Y.O., Oloniiju, S.D., Kasali, K.B., Akolade, M.T., Nonsimilar solution of a boundary layer flow of a Reiner–Philippoff fluid with nonlinear thermal convection, *Heat Transfer*, 51(6), 2022, 5659-5678.

[27] Saleem, K.B., Marafie, A.H., Al-Farhany, K., Hussam, W.K., Sheard, G.J., Natural convection heat transfer in a nanofluid filled l-shaped enclosure with time-periodic temperature boundary and magnetic field, *Alexandria Engineering Journal*, 69, 2023, 177-191.

[28] Bittencourt, F.L.F., Debenest, G., Martins, M.F., Free convection development caused by bed shrinkage in a vacuum-induced smoldering reactor, *Chemical Engineering Journal*, 430, 2022, 132847.

[29] Bilal, M., Ayed, H., Saeed, A., Brahmia, A., Gul, T., Kumam, P., The parametric computation of nonlinear convection magnetohydrodynamic nanofluid flow with internal heating across a fixed and spinning disk, *Waves in Random and Complex Media*, 2022, 1-16.

[30] Nasir, M., Waqas, M., Kausar, M.S., Bég, O.A., Zamri, N., Cattaneo-Christov dual diffusive non-Newtonian nanoliquid flow featuring nonlinear convection, *Chinese Journal of Physics*, 89, 2024, 1164-1181.

[31] Kukreja, H., Bharath, N., Siddesh, C.S., Kuldeep, S., An introduction to artificial neural network, *International Journal of Advance Research and Innovative Ideas in Education*, 1, 2016, 27-30.

[32] Morimoto, M., Fukami, K., Zhang, K., Fukagata, K., Generalization techniques of neural networks for fluid flow estimation, *Neural Computing and Applications*, 2022, 1-23.

[33] Li, A., Yuen, A.C.Y., Wang, W., Chen, T.B.Y., Lai, C.S., Yang, W., Wu, W., Chan, Q.N., Kook, S., Yeoh, G.H., Integration of computational fluid dynamics and artificial neural network for optimization design of battery thermal management system, *Batteries*, 8(7), 2022, 69.

[34] Affonso, R.R., Dam, R.S., Salgado, W.L., da Silva, A.X., Salgado, C.M., Flow regime and volume fraction identification using nuclear techniques, artificial neural networks and computational fluid dynamics, *Applied Radiation and Isotopes*, 159, 2020, 109103.

[35] Mulashani, A.K., Shen, C., Nkurlu, B.M., Mkono, C.N., Kawamala, M., Enhanced group method of data handling (GMDH) for permeability prediction based on the modified Levenberg Marquardt technique from well log data, *Energy*, 239, 2022, 121915.

[36] Lv, C., Xing, Y., Zhang, J., Na, X., Li, Y., Liu, T., Wang, F.Y., Levenberg–Marquardt backpropagation training of multilayer neural networks for state estimation of a safety-critical cyber-physical system, *IEEE Transactions on Industrial Informatics*, 14(8), 2017, 3436-3446.

[37] Raja, M.A.Z., Shoaib, M., Tabassum, R., Khan, N.M., Kehili, S., Bafakeeh, O.T., Stochastic numerical computing for entropy optimized of Darcy-Forchheimer nanofluid flow: Levenberg Marquardt Algorithm, *Chemical Physics Letters*, 807, 2022, 140070.

[38] Rehman, K.U., Shatanawi, W., Çolak, A.B., Computational Analysis on Magnetized and Non-Magnetized Boundary Layer Flow of Casson Fluid Past a Cylindrical Surface by Using Artificial Neural Networking, *Mathematics*, 11(2), 2023, 326.

[39] Aljohani, J.L., Alaidarous, E.S., Raja, M.A.Z., Alhothuali, M.S., Shoaib, M., Backpropagation of Levenberg Marquardt artificial neural networks for wire coating analysis in the bath of Sisko fluid, *Ain Shams Engineering Journal*, 12(4), 2021, 4133-4143.

[40] Sulaiman, M., Khan, N.A., Alshammari, F.S., Laouini, G., Performance of heat transfer in micropolar fluid with isothermal and isoflux boundary conditions using supervised neural networks, *Mathematics*, 11(5), 2023, 1173.

[41] Dholey, S., Unsteady separated stagnation-point flows and heat transfer over a plane surface moving normal to the flow impingement, *International Journal of Thermal Sciences*, 163, 2021, 106688.

[42] Lok, Y.Y., Pop, I., Stretching or shrinking sheet problem for unsteady separated stagnation-point flow, *Meccanica*, 49, 2014, 1479-1492.

[43] Wang, C.Y., Stagnation flow towards a shrinking sheet, *International Journal of Non-Linear Mechanics*, 43(5), 2008, 377-382.

[44] Nasir, S., Berrouk, A.S., Aamir, A., Gul, T., Ali, I., Features of flow and heat transport of MoS2+ GO hybrid nanofluid with nonlinear chemical reaction, radiation and energy source around a whirling sphere, *Heliyon*, 9(4), 2023, e15089.

[45] Salawu, S.O., Obalalu, A.M., Okoya, S.S., Thermal convection and solar radiation of electromagnetic actuator Cu–Al2O3/C3H8O2 and Cu–C3H8O2 hybrid nanofluids for solar collector optimization, *Materials Today Communications*, 33, 2022, 104763.

[46] Acharya, N., Öztop, H.F., On the entropy analysis and hydrothermal behavior of buoyancy-driven magnetized hybrid nanofluid flow within a semi-circular chamber fitted with a triangular heater: Application to thermal energy storage for energy management, *Numerical Heat Transfer, Part A: Applications*, 2023, 1-31.

[47] Acharya, N., On the hydrothermal behavior and entropy analysis of buoyancy driven magnetohydrodynamic hybrid nanofluid flow within an octagonal enclosure fitted with fins: Application to thermal energy storage, *Journal of Energy Storage*, 53, 2022, 105198.

[48] Alharbi, S.O., Gul, T., Khan, I., Khan, M.S., Alzahrani, S., Irreversibility Analysis through Neural Networking of the Hybrid Nanofluid for the Solar Collector Optimization, *Scientific Reports*, 13, 2023, 13350.

[49] Ishak, A., Lok, Y.Y., Pop, I., Stagnation-point flow over a shrinking sheet in a micropolar fluid, *Chemical Engineering Communications*, 197(11), 2010, 1417-1427.

ORCID iD

Arshad Khan 🆔 https://orcid.org/ 0000-0002-8694-2546

Taza Gul 🆔 https://orcid.org/0000-0003-1376-8345